Consistent lifting relations for the initialization of total-energy double-distribution-function kinetic models

Yiming Qi (岐亦铭),[1] Lian-Ping Wang (王连平),[2,*] Zhaoli Guo (郭照立),[3] and Shiyi Chen (陈十一)[4,2,1]

[1]*State Key Laboratory for Turbulence and Complex Systems, College of engineering, Peking University, Beijing 100871, China*

[2]*Guangdong Provincial Key Laboratory of Turbulence Research and Applications, Center for Complex Flows and Soft Matter Research and Department of Mechanics and Aerospace Engineering, Southern University of Science and Technology, Shenzhen, Guangdong 518055, China*

[3]*Institute of Interdisciplinary Research for Mathematics and Applied Science, Huazhong University of Science and Technology, Wuhan, Hubei 430074, China*

[4]*Eastern Institute for Advanced Study, Eastern Institute of Technology, Ningbo, Zhejiang 315200, China*

(Received 17 May 2023; accepted 9 November 2023; published 4 December 2023)

A lifting relation connecting the distribution function explicitly with the hydrodynamic variables is necessary for the Boltzmann equation-based mesoscopic approaches in order to correctly initialize a nonuniform hydrodynamic flow. We derive two lifting relations for Guo *et al.*'s total-energy double-distribution-function (DDF) kinetic model [Z. L. Guo *et al.*, Phys. Rev. E **75**, 036704 (2007)], one from the Hermite expansion of the conserved and nonconserved moments, and the second from the $O(\tau)$ Chapman-Enskog (CE) approximation of the Maxwellian exponential equilibrium. While both forms are consistent to the compressible Navier-Stokes-Fourier system theoretically, we stress that the latter may introduce numerical oscillations under the recently optimized discrete velocity models [Y. M. Qi *et al.*, Phys. Fluids **34**, 116101 (2022)], namely a 27 discrete velocity model of the seventh-order Gauss-Hermite quadrature (GHQ) accuracy (D3V27A7) for the velocity field combined with a 13 discrete velocity model of the fifth-order GHQ accuracy (D3V13A5) for the total energy. It is shown that the Hermite-expansion–based lifting relation can be alternatively derived from the latter approach using the truncated Hermite-polynomial equilibrium. Additionally, a relationship between the order of CE expansions and the truncated order of Hermite equilibria is developed to determine the minimal order of a Hermite equilibria required to recover any multiple-timescale macroscopic system. Next, three-dimensional compressible Taylor-Green vortex flows with different initial conditions and Ma numbers are simulated to demonstrate the effectiveness and potential issues of these lifting relations. The Hermite-expansion–based lifting relation works well in all cases, while the Chapman-Enskog-expansion–based lifting relation may produce numerical oscillations and a theoretical model is developed to predict such oscillations. Furthermore, the corresponding lifting relations for Qi *et al.*'s total energy DDF model [Y. M. Qi *et al.*, Phys. Fluids **34**, 116101 (2022)] are derived, and additional simulations are performed to illustrate the generality of our approach.

DOI: 10.1103/PhysRevE.108.065301

I. INTRODUCTION

Compared to the traditional computational fluid dynamics (CFD) methods solving directly the Navier-Stokes-Fourier (NSF) system, the Boltzmann-equation–based mesoscopic CFD methods, such as the lattice Boltzmann method (LBM) [1], the unified gas kinetic scheme (UGKS) [2], and the discrete unified gas kinetic scheme (DUGKS) [3], instead solve a model Boltzmann equation (i.e., the kinetic model). In the limit of small Knudsen number, which is of the primary interest here, these methods amount to solving the NSF system. While these mesoscopic methods have the advantage of addressing noncontinuum flows, as an approach living in the higher-dimensional configuration space, they all require a proper initialization of a number of discrete distribution functions based on the initial hydrodynamic conditions. The number of hydrodynamic variables is typically significantly less than the number of distribution functions involved in the kinetic model; therefore, specifying these distribution functions from the knowledge of the hydrodynamic variables is an underdetermined problem, which here is referred to as the lifting relation [4]. Specifically, the distribution functions in the Boltzmann-equation based methods involve both hydrodynamics variables and their spatial gradients according to the Chapman-Enskog (CE) expansion [5]. Although the existing literature has discussed several lifting relations, their consistency and implications to robust numerical simulations have not been carefully discussed; in particular, their performances in turbulent flow simulations have not been carefully examined.

The existing lifting relations or initialization methods have primarily concerned the incompressible viscous flows, and they can be roughly divided into three groups, i.e., the potentially costly iterative approach [6], the Hermite-expansion-based lifting relations [7,8], and the

*wanglp@sustech.edu.cn

Chapman-Enskog-expansion-based lifting relations [4,9–11]. First, the iterative approach relies on numerical iterations of the lattice Boltzmann equation under the constraints of initial hydrodynamic conditions. For example, Mei *et al.* [6] obtained the initial distribution functions by evolving the lattice Boltzmann equation while constraining the hydrodynamic velocity field in the equilibrium distribution, and this iterative process yields the correct pressure field equivalent to solving the pressure Poisson equation. The number of iterations could be large for a nonuniform turbulent initial flow. Similarly, van Leemput *et al.* [12] fixed the known conserved moments at every iteration in the moment space, which are naturally suited for the multiple-relaxation-time (MRT) LBM method. The number of iterative steps is typically of the order of 1000 for the initialization of two-dimensional Taylor-Green vortex flow [6]. Three-dimensional (3D) simulations could require more iterations for proper initialization.

Second, the Hermite-expansion–based lifting relations express the equilibrium part of the distribution functions in terms of conserved hydrodynamic variables and the nonequilibrium part in terms of nonconserved moments such as the viscous stress and heat flux. Krüger *et al.* [7] specified the nonequilibrium part of the distribution functions in terms of the viscous stress tensor when solving the force-free Boltzmann-Bhatnagar-Gross-Krook (Boltzmann-BGK) equation [13] for isothermal viscous flows. Tong *et al.* [8] derived the nonequilibrium part of the distribution function for the forced Boltzmann-BGK equation and applied their lifting relations in a multiscale approach combining LBM and molecular dynamics simulation. This approach may not be self sufficient as it requires prior knowledge of the constitutive relations for the nonconserved moments.

Third, the Chapman-Enskog-expansion–based lifting relations are typically derived by first expanding the distribution functions to a specific order in terms of the Knudsen number or other small parameter, converting all the time and space derivatives of the equilibrium distribution functions into the spatial derivatives of the hydrodynamics variables by the hydrodynamic equations, and then dropping certain terms judged to be insignificant. In this process, this approach provides the constitutive relations for the nonconserved moments. Skordos [9] proposed an approximate expression for the nonequilibrium part of the distribution based on the first-order CE expansion, for the force-free Boltzmann-BGK equation, and retained only the terms up to $O(\mathrm{Ma})$ for low-Mach-number flows. Imamura *et al.* [10] provided a more rigorous derivation of the nonequilibrium distribution based on the first-order CE expansion of the force-free Boltzmann-BGK equation and showed that the nonequilibrium distribution is proportional to the strain-rate tensor. To better realize the momentum conservation in the lifting relations, Xu *et al.* [4] performed the second-order CE expansion of the force-free Boltzmann-BGK equation and discarded the terms of $O(\mathrm{Ma}^2)$ for low Mach-number ($\mathrm{Ma} \leqslant 0.2$) weakly compressible flows. Tong *et al.* [11] extended the first-order CE analysis to the passive-scalar distribution function. Due to the discretization errors, they [14] later claimed that the second-order CE expansion of the lattice Boltzmann equation should be used to construct the lifting relations in order to be more consistent with the momentum equation.

Moreover, the CE expansions are not always limited to the distribution function. Salimi *et al.* [15] considered the second-order CE expansion of the force-free MRT lattice-Boltzmann equation in the moment space and expressed the distribution moments in terms of the equilibrium moments and their derivatives. Overall, these previous studies concern mainly the incompressible flow.

In contrast to the incompressible flow where the energy equation is not present, the mesoscopic methods for the thermal compressible flow involve the energy equation in addition to the mass and momentum equations. To make these mesoscopic methods computationally efficient, a second reduced distribution is introduced in order to describe the internal energy or temperature field, known as the double-distribution-function (DDF) approach. Depending on the specific definition of this second reduced distribution, there are several variations of the DDF approach, for example, the total-energy DDF approach [16], and the partial-internal-energy DDF approach [17]. For the DDF approach, the first reduced distribution function handles the mass and the momentum as in the incompressible flow, while the design of the second reduced distribution function and its equilibrium affects the required Gauss-Hermite quadrature (GHQ) accuracy [18–20]. With respect to the computational cost, the total energy DDF approach, which utilizes two sets of 3D *off-lattice* discrete particle velocity models (see Appendix A), namely a 27 discrete velocity model of the seventh-order GHQ accuracy (D3V27A7) [21,22] combined with a 13 discrete velocity model of the fifth-order GHQ accuracy (D3V13A5) [22], is currently the most efficient discrete velocity model [19,20]. The proper lifting relations in the DDF approach for compressible flows have not been systematically studied.

In the absence of discretization and Hermite expansion errors, the recovery of the NSF system would require the $O(\tau)$ CE approximation for the distribution functions, which amounts to the requirement of computing the velocity moments of the equilibrium distributions and their derivatives up to specific orders. It must be noted that the required order of the Hermite expansion of the equilibrium distributions must be carefully designed according to the detailed expressions of the different terms in the $O(\tau)$ CE expansion as well as the rigorous computation of all the nonequilibrium moments, as shown in Table I. Specifically, as we shall show that each time derivative of the equilibrium distribution could reduce the accuracy order of the Hermite expansion by one order, as implied by the multiple timescales (e.g., the advection timescale, diffusion timescale, and other slower timescales) of the physical problem. This subtle detail, if not fully observed, could lead to incorrect lifting relations based on the CE expansion.

In this work, we shall derive the lifting relations using two alternative approaches to illustrate the importance of matching the resulting lifting relations with the GHQ accuracy order of the particle velocity model, as well as explaining a source of numerical oscillations in one form of the lifting relations caused by high-order Hermite expansion terms. Then 3D compressible turbulence with a nonuniform initial flow, as specified by the 3D Taylor-Green vortex problem, is simulated using two alternative kinetic models [19,20] to demonstrate the optimal and correct choice of the lifting relations.

TABLE I. The required order of the Hermite expansion of the distributions in different DDF formulations in order to recover the NSF system. g is the first reduced distribution with its equilibrium $g^{\rm eq}$, and h is the second reduced distribution with its equilibrium $h^{\rm eq}$.

Approach	Total-energy DDF		Partial-internal-energy DDF	
Terms	Viscous stress	Heat flux	Viscous stress	Heat flux
g	2	2	2	3
h	Not used	1	Not used	1
$g^{\rm eq}$	3	3	3	4
$h^{\rm eq}$	Not used	2	Not used	2

The remainder of this paper is organized as follows. After a description of the macroscopic model (Sec. II A), Guo *et al.*'s total energy DDF mesoscopic model (Sec. II B), and the DUGKS approach (Sec. II C), we present the detailed derivations and inter-comparisons of the Hermite-expansion–based lifting relation (Sec. III A), the Chapman-Enskog-expansion–based lifting relation (Sec. III B), and the CE expansions for the truncated Hermite polynomial equilibria (Sec. III C). In Sec. IV, numerical results of compressible flow using different lifting relations are presented and compared. Section V summarizes our work and key conclusions. Appendices A–E provide a description of the discrete particle velocity models D3V13A5 and D3V27A7 (Appendix A), a brief introduction for Qi *et al.*'s total energy DDF model along with the corresponding numerical results (Appendix B), the implementation of the sixth-order targeted essentially nonoscillatory (TENO) scheme [23] (Appendix C), the essential details of Hermite polynomials (Appendix D), and the discussions of the Hermite expansions for the external force terms (Appendix E).

II. THE KINETIC MODEL AND NUMERICAL METHOD

A. Macroscopic governing equations

Different from the incompressible flow that treats temperature as a passive scalar, temperature in the energy equation for a compressible flow is closely coupled with the mass and momentum conservations. For example, the Euler equations describing continuum compressible flow of an ideal gas, without nonequilibrium effects, are written in the form of

$$\partial_t \rho + \nabla\cdot(\rho \boldsymbol{u}) = 0, \tag{1a}$$

$$\partial_t(\rho \boldsymbol{u}) + \nabla\cdot(\rho \boldsymbol{u}\boldsymbol{u}) = -\nabla p + \rho \boldsymbol{b}, \tag{1b}$$

$$\partial_t(\rho E) + \nabla\cdot(\rho E \boldsymbol{u}) = -\nabla\cdot(p\boldsymbol{u}) + \rho \boldsymbol{u}\cdot\boldsymbol{b}, \tag{1c}$$

where $\rho(\boldsymbol{x}, t)$ is the density, $\boldsymbol{x} = (x_1, \ldots, x_D)$ is the position in D-dimensional space, where D is the space dimension of the hydrodynamics variables, t is the time, $\boldsymbol{u}$ is the macroscopic velocity, $\boldsymbol{b}$ is the external force, p is the pressure, $E = \frac{1}{2}u^2 + e$ is the total energy per unit mass including the kinetic energy and the internal energy per unit mass $e = C_v T$, T is the temperature, and C_v is the specific heat capacity at constant volume. The ideal-gas equation of state (EOS), i.e., $p = \rho R T$, is used where R is the specific gas constant. When the viscous effect and thermal diffusion are considered, the macroscopic equations are amended from the Euler equations Eq. (1) to the NSF system, namely

$$\partial_t \rho + \nabla\cdot(\rho \boldsymbol{u}) = 0, \tag{2a}$$

$$\partial_t(\rho \boldsymbol{u}) + \nabla\cdot(\rho \boldsymbol{u}\boldsymbol{u}) = -\nabla p + \nabla\cdot\boldsymbol{\sigma} + \rho \boldsymbol{b}, \tag{2b}$$

$$\partial_t(\rho E) + \nabla\cdot(\rho E \boldsymbol{u}) = -\nabla\cdot\boldsymbol{q} - \nabla\cdot(p\boldsymbol{u}) + \nabla\cdot(\boldsymbol{\sigma}\cdot\boldsymbol{u}) + \rho \boldsymbol{u}\cdot\boldsymbol{b}, \tag{2c}$$

where the Newtonian viscous stress tensor $\boldsymbol{\sigma}$ and the heat flux $\boldsymbol{q}$, up to the order of $O(\tau)$, are given as

$$\boldsymbol{\sigma} = 2\mu(\boldsymbol{S} - \boldsymbol{I}\vartheta/D) + \mu_V \vartheta \boldsymbol{I}, \quad \boldsymbol{q} = -\kappa \nabla T. \tag{3}$$

Here $\mu = \rho\nu$ is the dynamic viscosity and ν is the kinematic viscosity, $\boldsymbol{S} = [\nabla\boldsymbol{u} + (\nabla\boldsymbol{u})^T]/2$ is the strain rate tensor, $\boldsymbol{I}$ is the identity tensor, μ_V is the bulk viscosity, $\vartheta = \nabla\cdot\boldsymbol{u}$ is the dilatation, $\kappa = \mu C_p/\mathrm{Pr}$ is the thermal conductivity coefficient given in terms of the Prandtl number Pr, and C_p is the specific heat capacity at constant pressure. Assuming air as the working fluid, we employ Sutherland's law [24] here, which has the following form:

$$\frac{\mu}{\mu_s} = \frac{1.4042(T/T_s)^{1.5}}{(T/T_s) + 0.40417}, \tag{4}$$

where $\mu_s = 1.716 \times 10^{-5}$ kg/(m s) is the air dynamic viscosity at the reference temperature $T_s = 273.15$ K.

The key idea in developing various kinetic models for a continuum flow is to use the NSF equations Eq. (2) as the design constraints [25]. Here we consider two specific total-energy DDF models that can accommodate arbitrary Prandtl numbers. The first is Guo *et al.*'s total-energy DDF model [16], which has recently been re-examined in the framework of DUGKS [20], where the bulk-to-shear viscosity ratio $\chi = \mu_V/\mu$ is fixed to $2[1/D - 1/(K+3)]$ once the internal degree of freedom K is specified. The second model is Qi *et al.*'s total energy DDF model, in which the bulk-to-shear viscosity ratio is a free parameter in its design. Guo *et al.* adjust the Prandtl number by introducing a separate relaxation time for the energy distribution function, while Qi *et al.* accomplishes this goal by designing a source term using a single relaxation time. Both kinetic models properly recover the NSF system under the CE analysis. We shall briefly introduce Guo *et al.*'s model [20] in the following section, while Qi *et al.*'s model [19] is summarized in Appendix B.

B. Guo *et al.*'s total energy double-distribution-function model

Guo *et al.*'s model starts with the Boltzmann-BGK equation [13],

$$\partial_t f + \boldsymbol{\xi}\cdot\nabla f + \boldsymbol{b}\cdot\nabla_{\boldsymbol{\xi}} f = -\tfrac{1}{\tau}(f - f^{\rm eq}), \tag{5}$$

where $f(\boldsymbol{x}, \boldsymbol{\xi}, \boldsymbol{\eta}, \boldsymbol{\zeta}, t)$ is the density distribution function, $\boldsymbol{\xi} = (\xi_1, \ldots, \xi_D)$ is the particle velocity in the D-dimensional subspace as indicated by $\boldsymbol{x}$, $\boldsymbol{\eta}$ is the particle velocity in the

remaining $(3-D)$-dimensional space, $\boldsymbol{\zeta}=(\zeta_1,\ldots,\zeta_K)$ denotes an internal kinetic variable of dimension K whose main purpose is to adjust the specific heat ratio γ, $\nabla_{\boldsymbol{\xi}}$ is the nabla operator in the $\boldsymbol{\xi}$ phase space, and $\tau=\mu/p$ is the relaxation time. The equilibrium distribution f^{eq} takes the standard Maxwellian form

$$f^{\mathrm{eq}}(\boldsymbol{x},\boldsymbol{\xi},\boldsymbol{\eta},\boldsymbol{\zeta},t)=\frac{\rho}{(2\pi RT)^{(K+3)/2}}\exp\left(-\frac{c^2+\eta^2+\zeta^2}{2RT}\right), \tag{6}$$

where $\boldsymbol{c}=\boldsymbol{\xi}-\boldsymbol{u}$ is the thermal fluctuating velocity. With the given equilibrium distribution, it follows that $C_v=(3+K)R/2$ and the specific heat at constant pressure $C_p=C_v+R=(5+K)R/2$, yielding a specific heat ratio $\gamma=C_p/C_v=(K+5)/(K+3)$. The conservative variables are determined by the moments of the distribution function and its equilibrium as

$$\begin{aligned}\rho&=\int f d\boldsymbol{\xi}d\boldsymbol{\eta}d\boldsymbol{\zeta}=\int f^{\mathrm{eq}}\,d\boldsymbol{\xi}d\boldsymbol{\eta}d\boldsymbol{\zeta},\\ \rho\boldsymbol{u}&=\int \boldsymbol{\xi} f d\boldsymbol{\xi}d\boldsymbol{\eta}d\boldsymbol{\zeta}=\int \boldsymbol{\xi} f^{\mathrm{eq}}\,d\boldsymbol{\xi}d\boldsymbol{\eta}d\boldsymbol{\zeta},\\ \rho E&=\frac{1}{2}\rho u^2+\rho e=\int\frac{\xi^2+\eta^2+\zeta^2}{2}f d\boldsymbol{\xi}d\boldsymbol{\eta}d\boldsymbol{\zeta}\\ &=\int\frac{\xi^2+\eta^2+\zeta^2}{2}f^{\mathrm{eq}}\,d\boldsymbol{\xi}d\boldsymbol{\eta}d\boldsymbol{\zeta}.\end{aligned} \tag{7}$$

Matching the moment equations of f with the NSF system, it can be shown that the viscous stress $\boldsymbol{\sigma}$ and the heat flux $\boldsymbol{q}$ should be evaluated as

$$\begin{aligned}\boldsymbol{\sigma}&=-\int \boldsymbol{cc}(f-f^{\mathrm{eq}})d\boldsymbol{\xi}d\boldsymbol{\eta}d\boldsymbol{\zeta},\\ \boldsymbol{q}&=\int \boldsymbol{c}\frac{c^2+\eta^2+\zeta^2}{2}f d\boldsymbol{\zeta}d\boldsymbol{\eta}d\boldsymbol{\xi}.\end{aligned} \tag{8}$$

To remove the internal degrees of freedom, we introduce two reduced distributions,

$$g(\boldsymbol{x},\boldsymbol{\xi},t)\equiv\int f(\boldsymbol{x},\boldsymbol{\xi},\boldsymbol{\eta},\boldsymbol{\zeta},t)d\boldsymbol{\eta}d\boldsymbol{\zeta}, \tag{9a}$$

$$h(\boldsymbol{x},\boldsymbol{\xi},t)\equiv\int\frac{\xi^2+\eta^2+\zeta^2}{2}f(\boldsymbol{x},\boldsymbol{\xi},\boldsymbol{\eta},\boldsymbol{\zeta},t)d\boldsymbol{\eta}d\boldsymbol{\zeta}. \tag{9b}$$

The collision kernel for the total energy distribution in Guo *et al.*'s model [16] is divided into the mechanical energy part and the internal energy part with two distinct relaxation times in order to handle an arbitrary Prandtl number. Namely, the corresponding Boltzmann-BGK equations for the two reduced distributions in Eq. (9) are generalized to

$$\partial_t g+\boldsymbol{\xi}\cdot\nabla g+\boldsymbol{b}\cdot\nabla_{\boldsymbol{\xi}}g=-\frac{1}{\tau_g}(g-g^{\mathrm{eq}}), \tag{10a}$$

$$\begin{aligned}\partial_t h+\boldsymbol{\xi}\cdot\nabla h+\boldsymbol{b}\cdot\nabla_{\boldsymbol{\xi}}h=&-\frac{1}{\tau_h}[h-h^{(eq)}]\\ &+\frac{Z}{\tau_{hg}}[g-g^{(eq)}]+\boldsymbol{b}\cdot\boldsymbol{\xi}g,\end{aligned} \tag{10b}$$

where τ_g and τ_h are two relaxation times relating to the momentum and energy relaxations respectively, $\tau_g=\tau$, $\tau_h=\tau_g/\mathrm{Pr}$, $\tau_{hg}^{-1}=\tau_h^{-1}-\tau_g^{-1}$, and $Z=\boldsymbol{\xi}\cdot\boldsymbol{u}-u^2/2$. The two equilibrium distribution functions can be expressed as

$$\begin{aligned}g^{\mathrm{eq}}(\boldsymbol{x},\boldsymbol{\xi},t)&=\frac{\rho}{(2\pi RT)^{D/2}}\exp\left(-\frac{c^2}{2RT}\right),\\ h^{\mathrm{eq}}(\boldsymbol{x},\boldsymbol{\xi},t)&=\frac{(3-D+K)RT+\xi^2}{2}g^{\mathrm{eq}}.\end{aligned} \tag{11}$$

In terms of the reduced distributions, the conservative variables, the viscous stress, and the heat flux become

$$\rho=\int g d\boldsymbol{\xi},\quad \rho\boldsymbol{u}=\int\boldsymbol{\xi}g d\boldsymbol{\xi},\quad \rho E=\int h d\boldsymbol{\xi}, \tag{12a}$$

$$\begin{aligned}\boldsymbol{\sigma}&=-\int\boldsymbol{cc}(g-g^{\mathrm{eq}})d\boldsymbol{\xi},\quad \boldsymbol{q}=\int\boldsymbol{c}(h-Zg)d\boldsymbol{\xi}\\ &=\int\boldsymbol{c}h d\boldsymbol{\xi}+\boldsymbol{u}\cdot(\boldsymbol{\sigma}-p\boldsymbol{I}).\end{aligned} \tag{12b}$$

To recover the macroscopic equations, we perform the CE analysis by taking τ_g and τ_h as small parameters. The CE expansions of Eq. (10) yield the following approximations for the two reduced distribution functions:

$$g=g^{\mathrm{eq}}-\tau_g(\partial_t+\boldsymbol{\xi}\cdot\nabla+\boldsymbol{b}\cdot\nabla_{\boldsymbol{\xi}})g^{\mathrm{eq}}+O(\tau_g^2), \tag{13a}$$

$$\begin{aligned}h=h^{\mathrm{eq}}&-\tau_h[(\partial_t+\boldsymbol{\xi}\cdot\nabla+\boldsymbol{b}\cdot\nabla_{\boldsymbol{\xi}})h^{\mathrm{eq}}-\boldsymbol{b}\cdot\boldsymbol{\xi}g^{\mathrm{eq}}]\\ &-Z(\tau_g-\tau_h)(\partial_t+\boldsymbol{\xi}\cdot\nabla+\boldsymbol{b}\cdot\nabla_{\boldsymbol{\xi}})g^{\mathrm{eq}}+O(\tau_g^2,\tau_h^2).\end{aligned} \tag{13b}$$

If we truncate the expansions Eqs. (13a) and (13b) up to the order of $O(1)$, then the zeroth and the first-order velocity moment of g can lead to the mass conservation and the momentum conservation in Eqs. (1a) and (1b), respectively, and the zeroth-order velocity moment of h can recover the energy equation in Eq. (1c). Moreover, if we truncate the expansions Eqs. (13a) and (13b) up to the order of $O(\tau)$ and refine the aforementioned velocity moments, then the NSF system, Eq. (2), can be recovered.

For the best computation efficiency, Guo *et al.* [20] utilized two different 3D *off-lattice* discrete particle velocity models, D3V27A7 and D3V13A5, for the two reduced distributions g and h, respectively. Thus, a total of only 40 discrete particle distributions are solved. Here D3V27A7 denotes a particle velocity model in 3D space with 27 discrete velocities and seventh-order GHQ accuracy; likewise, D3V13A5 is a particle velocity model in 3D space with 13 discrete velocities and fifth-order GHQ accuracy. Therefore, the g-related terms in Eq. (10b) should be projected to the D3V13A5 particle velocity space. The CE analysis of the energy distribution, specifically the heat flux moment at the NSF level, indicates that moments up to the second order of g are needed when recovering the energy equation, which is equivalent to the requirement of moments of g^{eq} up to the third order. This then implies the following Hermite projection [20] can be used

$$\begin{aligned}\frac{Z}{\tau_{hg}}[g-g^{(\mathrm{eq})}]&=\frac{1-\mathrm{Pr}^{-1}}{\tau_h}Z[g-g^{(\mathrm{eq})}]\\ &\approx\frac{\mathrm{Pr}^{-1}-1}{\tau_h}\omega(\boldsymbol{\xi},T_0)\frac{\boldsymbol{\xi}\cdot\boldsymbol{\sigma}\cdot\boldsymbol{u}}{RT_0},\end{aligned} \tag{14}$$

where $\omega(\boldsymbol{\xi}, T_0) = \exp[-\xi^2/(2RT_0)]/(2\pi RT_0)^{D/2}$ is the weighting function and T_0 is the constant reference temperature.

C. The DUGKS approach

The numerical simulations to be conducted in this study utilizes the DUGKS approach. A brief description of the DUGKS approach for solving the force-free total energy DDF model is provided here. For convenience, we write Eqs. (10a) and (10b) in a unified form,

$$\partial_t \phi + \boldsymbol{\xi} \cdot \nabla \phi = -\tfrac{1}{\tau_\phi}(\phi - \phi'), \tag{15}$$

where ϕ refers to either g or h and ϕ' equals g^{eq} and $h^{\mathrm{eq}} + (\mathrm{Pr}^{-1} - 1)\omega(\boldsymbol{\xi}, T_0)\boldsymbol{\xi} \cdot \boldsymbol{\sigma} \cdot \boldsymbol{u}/(RT_0)$, respectively. As a finite-volume scheme, the computational domain of DUGKS is discretized into many connected cells V_j with $\boldsymbol{x}_j$ denoting the positions of the cell centers. Integrating Eq. (15) over the cell V_j from time t_n to $t_{n+1} = t_n + \Delta t$ and applying the midpoint rule for the convective term $\boldsymbol{\xi} \cdot \nabla\phi$ and the trapezoidal rule for the collision term $-(\phi - \phi')/\tau_\phi$, we obtain

$$\tilde{\phi}_j^{n+1}(\boldsymbol{\xi}) = \tilde{\phi}_j^{+,n}(\boldsymbol{\xi}) - \frac{\Delta t}{|V_j|} J_\phi^{n+1/2}(\boldsymbol{\xi}), \tag{16}$$

where two linear transformations, $\tilde{\phi} = \phi - \frac{\phi' - \phi}{\tau_\phi}\frac{\Delta t}{2}$ and $\tilde{\phi}^+ = \phi + \frac{\phi' - \phi}{\tau_\phi}\frac{\Delta t}{2}$, are introduced to convert the implicit scheme to an explicit form. Here $\tilde{\phi}_j^n$, $\tilde{\phi}_j^{+,n}$, ϕ_j^n, and $(\phi')_j^n$ represent the cell-averaged values of $\tilde{\phi}(\boldsymbol{x}, \boldsymbol{\xi}, t_n)$, $\tilde{\phi}^+(\boldsymbol{x}, \boldsymbol{\xi}, t_n)$, $\phi(\boldsymbol{x}, \boldsymbol{\xi}, t_n)$, and $\phi'(\boldsymbol{x}, \boldsymbol{\xi}, t_n)$, respectively. The flux across the cell interface is given by

$$J_\phi^{n+1/2} = \oint_{\partial V_j} (\boldsymbol{\xi} \cdot \boldsymbol{n})\phi(\boldsymbol{x}, \boldsymbol{\xi}, t_{n+1/2}) dS, \tag{17}$$

where ∂V_j is the surface of V_j with the outward unit normal vector $\boldsymbol{n}$ and $t_{n+1/2} = t_n + \Delta t/2 \equiv t_n + \delta t$ denotes the half time step.

In the numerical implementation, we track $\tilde{\phi}$ instead of the original ϕ. The conservative variables, the viscous stress and the heat flux at the cell center can be calculated by $\tilde{\phi}$ as

$$\rho = \int \tilde{g} d\boldsymbol{\xi}, \quad \rho\boldsymbol{u} = \int \boldsymbol{\xi}\tilde{g} d\boldsymbol{\xi}, \quad \rho E = \int \tilde{h} d\boldsymbol{\xi}, \tag{18a}$$

$$\boldsymbol{\sigma} = \frac{2\tau_g}{2\tau_g + \Delta t} \int \boldsymbol{cc}(g^{\mathrm{eq}} - \tilde{g}) d\boldsymbol{\xi},$$

$$\boldsymbol{q} = \frac{2\tau_h}{2\tau_h + \Delta t} \int \boldsymbol{c}\tilde{h} d\boldsymbol{\xi} + \boldsymbol{u} \cdot (\boldsymbol{\sigma} - p\boldsymbol{I}). \tag{18b}$$

The computation of flux across the cell interface in Eq. (17) needs distribution functions at boundary nodes $\boldsymbol{x}_b$ at the half time step, which can be computed by integrating the Boltzmann equations, Eq. (15), along the characteristic line using the trapezoidal rule, namely

$$\begin{aligned}\phi(\boldsymbol{x}_b, \boldsymbol{\xi}, t_n + \delta t) - \phi(\boldsymbol{x}_b - \boldsymbol{\xi}\delta t, \boldsymbol{\xi}, t_n) \\ = \frac{\delta t}{2}\left[\left(\frac{\phi' - \phi}{\tau_\phi}\right)(\boldsymbol{x}_b, \boldsymbol{\xi}, t_n + \delta t) \right. \\ \left. + \left(\frac{\phi' - \phi}{\tau_\phi}\right)(\boldsymbol{x}_b - \boldsymbol{\xi}\delta t, \boldsymbol{\xi}, t_n)\right].\end{aligned} \tag{19}$$

Similarly, another two auxiliary distribution functions, namely $\bar{\phi} = \phi - \frac{\phi' - \phi}{\tau_\phi}\frac{\delta t}{2}$ and $\bar{\phi}^+ = \phi + \frac{\phi' - \phi}{\tau_\phi}\frac{\delta t}{2}$, are introduced to make the above explicit in time, giving

$$\begin{aligned}\bar{\phi}(\boldsymbol{x}_b, \boldsymbol{\xi}, t_n + \delta t) = \bar{\phi}^+(\boldsymbol{x}_b - \boldsymbol{\xi}\delta t, \boldsymbol{\xi}, t_n) \approx \bar{\phi}^+(\boldsymbol{x}_j, \boldsymbol{\xi}, t_n) \\ + (\boldsymbol{x}_b - \boldsymbol{x}_j - \boldsymbol{\xi}\delta t)\nabla\bar{\phi}^+(\boldsymbol{x}_j, \boldsymbol{\xi}, t_n),\end{aligned} \tag{20}$$

where $\bar{\phi}^+$ may be constructed by linear interpolations from the values at cell centers. To better capture the discontinuous structures such as shocklets in a compressible turbulence without introducing numerical oscillations, the gradient $\nabla\bar{\phi}^+(\boldsymbol{x}_j, \boldsymbol{\xi}, t_n)$ at the cell center is calculated by differencing the cell boundary values $\bar{\phi}^+(\boldsymbol{x}_b, \boldsymbol{\xi}, t_n)$ reconstructed from cell-averaged values,

$$\bar{\phi}_j^{+,n}(\boldsymbol{\xi}) = \frac{2\tau_\phi - \delta t}{2\tau_\phi + \Delta t}\tilde{\phi}_j^n(\boldsymbol{\xi}) + \frac{3\delta t}{2\tau_\phi + \Delta t}(\phi')_j^n(\boldsymbol{\xi}), \tag{21}$$

through a the sixth-order TENO scheme (see Appendix C).

The distribution function in the flux $J_\phi^{n+1/2}$ is obtained by

$$\begin{aligned}\phi(\boldsymbol{x}_b, \boldsymbol{\xi}, t_n + \delta t) = \frac{2\tau_\phi}{2\tau_\phi + \delta t}\bar{\phi}(\boldsymbol{x}_b, \boldsymbol{\xi}, t_n + \delta t) \\ + \frac{\delta t}{2\tau_\phi + \delta t}\phi'(\boldsymbol{x}_b, \boldsymbol{\xi}, t_n + \delta t),\end{aligned} \tag{22}$$

where the computation of $\phi'(\boldsymbol{x}_b, \boldsymbol{\xi}, t_n + \delta t)$ makes use of the variables at the cell interface at the half time step. These variables can be readily evaluated from Eq. (20) as

$$\begin{aligned}\rho(\boldsymbol{x}_b, t_n + \delta t) &= \int \bar{g} d\boldsymbol{\xi}, \quad (\rho\boldsymbol{u})(\boldsymbol{x}_b, t_n + \delta t) \\ &= \int \boldsymbol{\xi}\bar{g} d\boldsymbol{\xi}, \quad (\rho E)(\boldsymbol{x}_b, t_n + \delta t) \\ &= \int \bar{h} d\boldsymbol{\xi}, \quad \boldsymbol{\sigma}(\boldsymbol{x}_b, t_n + \delta t) \\ &= \frac{2\tau_g}{2\tau_g + \delta t}\int \boldsymbol{cc}(g^{\mathrm{eq}} - \bar{g}) d\boldsymbol{\xi}.\end{aligned} \tag{23}$$

The distribution function $\tilde{\phi}^+$ in Eq. (16) can be obtained by

$$\tilde{\phi}^+ = \tfrac{4}{3}\bar{\phi}^+ - \tfrac{1}{3}\tilde{\phi}. \tag{24}$$

Finally, Eq. (16) is used to compute $\tilde{\phi}_j^{n+1}(\boldsymbol{\xi})$.

The time step Δt is determined by the Courant-Friedricks-Lewy (CFL) condition,

$$\Delta t = \frac{\mathrm{CFL} \cdot \Delta x_{\min}}{u_{\max} + \xi_{\max}}, \tag{25}$$

where CFL is the CFL number, $\Delta x_{\min}$ is the minimal grid spacing, $u_{\max}$ is the maximal macroscopic velocity magnitude of $\boldsymbol{u}$, and $\xi_{\max}$ is the maximal particle velocity magnitude of $\boldsymbol{\xi}$.

III. THE DESIGN OF THE LIFTING RELATIONS

In this section, we discuss two approaches in constructing the lifting relations and compare their similarities and differences from the theoretical perspective. This sets the stage for them to be used as an initialization method for compressible flow simulations to be discussed in Sec. IV.

A. The Hermite-expansion–based lifting relation

Now we discuss the lifting relation based on the Hermite expansion alone. We divide each distribution function into the equilibrium part and the nonequilibrium part, namely $g = g^{\rm eq} + g^{\rm neq}$ and $h = h^{\rm eq} + h^{\rm neq}$. Relating the conservative variables, the viscous stress, and the heat flux in Eqs. (11) and (12) to the velocity moments of the equilibrium and nonequilibrium distribution functions, we obtain

$$\int g^{\rm eq}\,d\boldsymbol{\xi} = \rho, \quad \int \boldsymbol{\xi} g^{\rm eq}\,d\boldsymbol{\xi} = \rho\boldsymbol{u}, \quad \int \boldsymbol{\xi}\boldsymbol{\xi} g^{\rm eq}\,d\boldsymbol{\xi} = \rho\boldsymbol{u}\boldsymbol{u} + p\boldsymbol{I}, \tag{26a}$$

$$\int g^{\rm neq} d\boldsymbol{\xi} = 0, \quad \int \boldsymbol{\xi} g^{\rm neq} d\boldsymbol{\xi} = \boldsymbol{0}, \quad \int \boldsymbol{\xi}\boldsymbol{\xi} g^{\rm neq} d\boldsymbol{\xi} = -\boldsymbol{\sigma}, \tag{26b}$$

$$\int h^{\rm eq}\,d\boldsymbol{\xi} = \rho E, \quad \int \boldsymbol{\xi} h^{\rm eq}\,d\boldsymbol{\xi} = (\rho E + p)\boldsymbol{u},$$

$$\int h^{\rm neq} d\boldsymbol{\xi} = 0, \int \boldsymbol{\xi} h^{\rm neq} d\boldsymbol{\xi} = \boldsymbol{q} - \boldsymbol{\sigma}\cdot\boldsymbol{u}. \tag{26c}$$

Based on the $O(\tau)$ CE expansion, Eq. (13), recovering the viscous stress and the heat flux in Eq. (3) at the NSF level needs additional two velocity moments as follows:

$$\int \xi_i\xi_j\xi_k g^{\rm eq}\,d\boldsymbol{\xi} = \rho u_i u_j u_k + p u_i I_{jk} + p u_j I_{ik} + p u_k I_{ij}, \tag{27a}$$

$$\int \boldsymbol{\xi}\boldsymbol{\xi} h^{\rm eq}\,d\boldsymbol{\xi} = p(RT + E)\boldsymbol{I} + (2p + \rho E)\boldsymbol{u}\boldsymbol{u}. \tag{27b}$$

Now we shall construct the Hermite-expansion–based lifting relation for g^H and h^H from the above moments for g and h. By setting all the unmentioned moments to zero for convenience, the truncated Hermite expansions (see Appendix D) are

$$g^H = g^{\rm eq,(3)} + g^{\rm neq,(2)} = \omega(\boldsymbol{\xi}, T_0)\left[\sum_{n=0}^{3}\frac{1}{n!}\tilde{a}_i^{(n)}(g^{\rm eq})\mathcal{H}_i^{(n)}(\tilde{\boldsymbol{\xi}}) + \sum_{n=0}^{2}\frac{1}{n!}\tilde{a}_i^{(n)}(g^{\rm neq})\mathcal{H}_i^{(n)}(\tilde{\boldsymbol{\xi}})\right], \tag{28a}$$

$$h^H = h^{\rm eq,(2)} + h^{\rm neq,(1)} = \omega(\boldsymbol{\xi}, T_0)\left[\sum_{n=0}^{2}\frac{1}{n!}\tilde{a}_i^{(n)}(h^{\rm eq})\mathcal{H}_i^{(n)}(\tilde{\boldsymbol{\xi}}) + \sum_{n=0}^{1}\frac{1}{n!}\tilde{a}_i^{(n)}(h^{\rm neq})\mathcal{H}_i^{(n)}(\tilde{\boldsymbol{\xi}})\right], \tag{28b}$$

where $g^{\rm eq,(3)}$ and $g^{\rm neq,(2)}$ represent the third-order Hermite expansion of $g^{\rm eq}$ and the second-order Hermite expansion of $g^{\rm neq}$, respectively; $h^{\rm eq,(2)}$ and $h^{\rm neq,(1)}$ indicate the second-order Hermite expansion of $h^{\rm eq}$ and the first-order Hermite expansion of $h^{\rm neq}$, respectively; and $\tilde{a}_i^{(n)}(\phi)$ denotes the nth-order Hermite expansion coefficient of ϕ that can be computed by Eq. (D7). It is noted that, in each case, the equilibrium part and nonequilibrium part are handled separately, with the equilibrium part being expanded to one order higher in the Hermite expansion, as required by the CE analysis. The respective Hermite expansion coefficients follow from the moments in Eqs. (26) and (27), namely

$$\tilde{a}^{(0)}(g^{\rm eq}) = \rho, \quad \tilde{\boldsymbol{a}}^{(1)}(g^{\rm eq}) = \rho\frac{\boldsymbol{u}}{\sqrt{RT_0}}, \quad \tilde{\boldsymbol{a}}^{(2)}(g^{\rm eq}) = \rho\left[\frac{\boldsymbol{u}\boldsymbol{u}}{RT_0} + \left(\frac{T}{T_0} - 1\right)\boldsymbol{I}\right], \tag{29a}$$

$$\boldsymbol{a}_{ijk}^{(3)}(g^{\rm eq}) = \rho\left[\frac{u_i u_j u_k}{(RT_0)^{3/2}} + \left(\frac{T}{T_0} - 1\right)\frac{u_i I_{jk} + u_j I_{ki} + u_k I_{ij}}{\sqrt{RT_0}}\right], \tag{29b}$$

$$\tilde{a}^{(0)}(g^{\rm neq}) = 0, \quad \tilde{\boldsymbol{a}}^{(1)}(g^{\rm neq}) = \boldsymbol{0}, \quad \tilde{\boldsymbol{a}}^{(2)}(g^{\rm neq}) = -\frac{\boldsymbol{\sigma}}{RT_0}, \tag{29c}$$

$$\tilde{a}^{(0)}(h^{\rm eq}) = \rho E, \quad \tilde{\boldsymbol{a}}^{(1)}(h^{\rm eq}) = (\rho E + p)\frac{\boldsymbol{u}}{\sqrt{RT_0}}, \quad \tilde{\boldsymbol{a}}^{(2)}(h^{\rm eq}) = \rho E\left[\frac{\boldsymbol{u}\boldsymbol{u}}{RT_0} + \left(\frac{T}{T_0} - 1\right)\boldsymbol{I}\right] + \frac{T}{T_0}(2\rho\boldsymbol{u}\boldsymbol{u} + p\boldsymbol{I}), \tag{29d}$$

$$\tilde{a}^{(0)}(h^{\rm neq}) = 0, \quad \tilde{\boldsymbol{a}}^{(1)}(h^{\rm neq}) = \frac{\boldsymbol{q} - \boldsymbol{\sigma}\cdot\boldsymbol{u}}{\sqrt{RT_0}}. \tag{29e}$$

The above formal procedure then completes the construction of the lifting relation and we have

$$g^{\rm eq,(3)} = \omega(\boldsymbol{\xi}, T_0)\rho\left\{\begin{aligned}&1 + \frac{\boldsymbol{u}\cdot\boldsymbol{\xi}}{RT_0} + \frac{1}{2}\left[\left(\frac{\boldsymbol{u}\cdot\boldsymbol{\xi}}{RT_0}\right)^2 - \frac{u^2}{RT_0} + \left(\frac{T}{T_0} - 1\right)\left(\frac{\xi^2}{RT_0} - D\right)\right]\\ &+ \frac{\boldsymbol{u}\cdot\boldsymbol{\xi}}{6RT_0}\left\{\left(\frac{\boldsymbol{u}\cdot\boldsymbol{\xi}}{RT_0}\right)^2 + 3\left(\frac{T}{T_0} - 1\right)\left[\frac{\xi^2}{RT_0} - (D+2)\right] - \frac{3u^2}{RT_0}\right\}\end{aligned}\right\}, \tag{30a}$$

$$g^{\rm neq,(2)} = \frac{\omega(\boldsymbol{\xi}, T_0)}{2RT_0}\left[{\rm Tr}(\boldsymbol{\sigma}) - \frac{\boldsymbol{\xi}\cdot\boldsymbol{\sigma}\cdot\boldsymbol{\xi}}{RT_0}\right], \tag{30b}$$

$$h^{\mathrm{eq},(2)} = \omega(\boldsymbol{\xi}, T_0)\rho E\left\{1+\frac{\boldsymbol{u}\cdot\boldsymbol{\xi}}{RT_0}+\frac{1}{2}\left[\left(\frac{\boldsymbol{u}\cdot\boldsymbol{\xi}}{RT_0}\right)^2-\frac{u^2}{RT_0}+\left(\frac{T}{T_0}-1\right)\left(\frac{\xi^2}{RT_0}-D\right)\right]\right\} + \omega(\boldsymbol{\xi}, T_0)p\left\{\frac{\boldsymbol{u}\cdot\boldsymbol{\xi}}{RT_0}+\left(\frac{\boldsymbol{u}\cdot\boldsymbol{\xi}}{RT_0}\right)^2-\frac{u^2}{RT_0}+\frac{T}{2T_0}\left(\frac{\xi^2}{RT_0}-D\right)\right\}. \tag{30c}$$

$$h^{\mathrm{neq},(2)} = \frac{\omega(\boldsymbol{\xi}, T_0)}{RT_0}\boldsymbol{\xi}\cdot(\boldsymbol{q}-\boldsymbol{\sigma}\cdot\boldsymbol{u}), \tag{30d}$$

where $\mathrm{Tr}(\boldsymbol{\phi})$ means finding the trace of the tensor $\boldsymbol{\phi}$.

In summary, the above Hermite-expansion–based lifting relations identify, through the $O(\tau)$ CE expansion, the minimum set of moments required to derive the NSF system. This minimum set is also what we used to determine the minimum GHQ accuracy requirements of the discrete velocity models. Therefore, they are fully consistent with the GHQ accuracy of D3V27A7 and D3V13A5, namely they can be used to formally recover the viscous stress and heat flux precisely with these discrete velocity models. However, the exact constitutive relations for the viscous stress and the heat flux, such as Eq. (3), are not made explicit in the above procedure; they have to be worked out separately, for example, by the CE analysis (see the subsection below). Since the velocity moments for Guo *et al.*'s model are the same as these for Qi *et al.*'s model, the two models then share the same Hermite-expansion–based lifting relations, Appendix Eqs. (28) and (30), as shown in Appendix B. Furthermore, it can be shown that the lifting relations, Eqs. (28) and (30), satisfy the two reduced Boltzmann equations, Eq. (10), up to the order $O(\tau)$, as well as the two reduced Boltzmann equations with source terms, Eq. (B3), up to the order $O(\tau)$.

B. The Chapman-Enskog-expansion–based lifting relation

It is well known that the NSF system can be derived from the $O(\tau)$ CE analysis. In this process, the zeroth- and first-order velocity moments of the $O(\tau)$ approximation of Eq. (13a) yield the continuity equation and the Navier-Stokes equation, respectively, while the energy equation corresponds to the zeroth-order velocity moment of the $O(\tau)$ approximation of Eq. (13b). After utilizing the Euler equations, Eq. (1), to convert all the temporal derivatives in Eq. (13) into spatial derivatives and keeping all terms up to the $O(\tau)$ order, the following Chapman-Enskog-expansion–based lifting relations of the two reduced distributions, g^{CE} and h^{CE}, can be obtained

$$g^{\mathrm{CE}} = g^{\mathrm{eq}}\left\{1-\tau_g\left[\left(\frac{c^2}{2RT}-\frac{D+2}{2}\right)\boldsymbol{c}\cdot\nabla(\ln T)+\frac{\boldsymbol{c}\cdot\nabla\boldsymbol{u}\cdot\boldsymbol{c}}{RT}-\left(\frac{c^2}{RT}+K+3-D\right)\frac{\vartheta}{K+3}\right]\right\}, \tag{31a}$$

$$h^{\mathrm{CE}} = h^{\mathrm{eq}} - g^{\mathrm{eq}}\frac{\tau_g}{2}\left\{\begin{array}{l}\dfrac{(3-D+K)R}{\mathrm{Pr}}\left(\boldsymbol{c}\cdot\nabla-\dfrac{2\vartheta}{K+3}\right)T+\left[\dfrac{(3-D+K)RT+c^2}{\mathrm{Pr}}+u^2+2\boldsymbol{c}\cdot\boldsymbol{u}\right]\cdot \\ \left[\left(\dfrac{c^2}{2RT}-\dfrac{D+2}{2}\right)\boldsymbol{c}\cdot\nabla(\ln T)+\dfrac{\boldsymbol{c}\cdot\nabla\boldsymbol{u}\cdot\boldsymbol{c}}{RT}-\left(\dfrac{c^2}{RT}+K+3-D\right)\dfrac{\vartheta}{K+3}\right]\end{array}\right\}. \tag{31b}$$

It is noted that these results obtained from the CE analysis may require high-order GHQ accuracy of the discrete velocity models, as shown below.

Several comments can be made here for the two sets of the lifting relations. First, the lifting relations satisfy all the expected conserved velocity moments, the viscous stress moment, and the heat flux moment, namely

$$\rho = \int g^{\mathrm{CE}}d\boldsymbol{\xi} = \int g^{H}d\boldsymbol{\xi}, \quad \rho\boldsymbol{u} = \int \boldsymbol{\xi}g^{\mathrm{CE}}d\boldsymbol{\xi} = \int \boldsymbol{\xi}g^{H}d\boldsymbol{\xi}, \tag{32a}$$

$$\rho E = \int h^{\mathrm{CE}}d\boldsymbol{\xi} = \int h^{H}d\boldsymbol{\xi}, \tag{32b}$$

$$\boldsymbol{\sigma} = -\int \boldsymbol{cc}(g^{\mathrm{CE}}-g^{\mathrm{eq}})d\boldsymbol{\xi} = -\int \boldsymbol{cc}(g^{H}-g^{\mathrm{eq}})d\boldsymbol{\xi}, \tag{32c}$$

$$\boldsymbol{q} = \int \boldsymbol{c}(h^{\mathrm{CE}}-Zg^{\mathrm{CE}})d\boldsymbol{\xi} = \int \boldsymbol{c}(h^{H}-Zg^{H})d\boldsymbol{\xi}. \tag{32d}$$

The above moments ensure that the NSF system can be realized. In fact, all the moments in Eq. (26) are satisfied by Eq. (31). This implies that Eq. (31) is identical to the Hermite-expansion–based lifting relations, Eqs. (28) and (30), if Eq. (31) were projected onto the same truncated Hermite moments space. In other words, the only difference is that Eq. (31) contains some terms from the respective Hermite expansion at higher orders.

Second, for the reason expressed above, the required GHQ accuracy, with $\omega(\boldsymbol{\xi}, T_0)$ as the Gauss weighting function, is different for the two sets of the lifting relations. Specifically, the Chapman-Enskog–based lifting relation demands a higher-order GHQ accuracy in order to cleanly remove any potential contamination to the lower-order moments contained in Eq. (28), resulting

from numerical errors in treating higher-order moments. In other words, direct use of Eq. (31) in flow initialization in LBM or DUGKS with given discrete velocity models could introduce these numerical errors, as shown in Sec. IV A.

Specifically, we take the forms of Eq. (31) for the viscous stress and the heat flux, we obtain

$$\begin{aligned} p\boldsymbol{I}-\boldsymbol{\sigma} &= \int \boldsymbol{c}\boldsymbol{c}g^{\mathrm{CE}}d\boldsymbol{\xi} \\ &= \int \boldsymbol{c}\boldsymbol{c}g^{\mathrm{eq}}\left\{1-\tau_g\left[\left(\frac{c^2}{2RT}-\frac{D+2}{2}\right)\boldsymbol{c}\cdot\nabla(\ln T)+\frac{\boldsymbol{c}\cdot\nabla\boldsymbol{u}\cdot\boldsymbol{c}}{RT}-\left(\frac{c^2}{RT}+K+3-D\right)\frac{\vartheta}{K+3}\right]\right\}d\boldsymbol{\xi}, \end{aligned} \tag{33a}$$

$$\begin{aligned} \boldsymbol{q}+\boldsymbol{u}\cdot(p\boldsymbol{I}-\boldsymbol{\sigma}) &= \int \boldsymbol{c}h^{\mathrm{CE}}d\boldsymbol{\xi} \\ &= \int \boldsymbol{c}h^{\mathrm{eq}}\,d\boldsymbol{\xi}-\frac{\tau_g}{2}\int \boldsymbol{c}g^{\mathrm{eq}}\left\{\begin{array}{l}\dfrac{(3-D+K)R}{\mathrm{Pr}}\left(\boldsymbol{c}\cdot\nabla-\dfrac{2\vartheta}{K+3}\right)T+\left[\dfrac{(3-D+K)RT+c^2}{\mathrm{Pr}}+u^2+2\boldsymbol{c}\cdot\boldsymbol{u}\right]\cdot \\ \left[\left(\dfrac{c^2}{2RT}-\dfrac{D+2}{2}\right)\boldsymbol{c}\cdot\nabla(\ln T)+\dfrac{\boldsymbol{c}\cdot\nabla\boldsymbol{u}\cdot\boldsymbol{c}}{RT}-\left(\dfrac{c^2}{RT}+K+3-D\right)\dfrac{\vartheta}{K+3}\right]\end{array}\right\}d\boldsymbol{\xi}. \end{aligned} \tag{33b}$$

In Eq. (33a), the integrals related to the temperature gradient are equal to zero, but their precise computation needs at least a 10th-order GHQ accuracy. The integrals for the remaining parts of the right-hand side of Eq. (33a) require the 8th-order GHQ accuracy, which ensure the recovery of the constitutive relation $\boldsymbol{\sigma}=2\tau_g p(\boldsymbol{S}-\vartheta\boldsymbol{I}/(K+3))$. Futhermore, Eq. (33b) contains the following integral terms:

$$\int \boldsymbol{c}h^{\mathrm{eq}}\,d\boldsymbol{\xi}=p\boldsymbol{u},\quad \int \boldsymbol{c}g^{\mathrm{eq}}\left(\boldsymbol{c}\cdot\nabla-\frac{2\vartheta}{K+3}\right)T\,d\boldsymbol{\xi}=p\nabla T, \tag{34a}$$

$$\begin{aligned} &\int \boldsymbol{c}g^{\mathrm{eq}}\left[\frac{(3-D+K)RT+c^2}{\mathrm{Pr}}+u^2+2\boldsymbol{c}\cdot\boldsymbol{u}\right] \\ &\quad\times\left[\left(\frac{c^2}{2RT}-\frac{D+2}{2}\right)\boldsymbol{c}\cdot\nabla(\ln T)+\frac{\boldsymbol{c}\cdot\nabla\boldsymbol{u}\cdot\boldsymbol{c}}{RT}-\left(\frac{c^2}{RT}+K+3-D\right)\frac{\vartheta}{K+3}\right]d\boldsymbol{\xi} \\ &=\int g^{\mathrm{eq}}\left\{\left[\frac{(3-D+K)RT+c^2}{\mathrm{Pr}}+u^2\right]\left(\frac{c^2}{2RT}-\frac{D+2}{2}\right)\boldsymbol{c}\boldsymbol{c}\cdot\nabla(\ln T)\right. \\ &\quad\left.+2\left[\frac{\boldsymbol{c}\cdot\nabla\boldsymbol{u}\cdot\boldsymbol{c}}{RT}-\left(\frac{c^2}{RT}+K+3-D\right)\frac{\vartheta}{K+3}\right]\boldsymbol{c}\boldsymbol{c}\cdot\boldsymbol{u}\right\}d\boldsymbol{\xi}, \end{aligned} \tag{34b}$$

where the eliminations of the highest odd-order velocity moments of g^{eq} in Eq. (34b) require the 10th-order GHQ accuracy. And the part involving the temperature gradient should be calculated using the 12th-order GHQ accuracy to yield the correct heat flux expression

$$\int g^{\mathrm{eq}}\left[\frac{c^4}{2\mathrm{Pr}RT}+\left(\frac{u^2}{2RT}+\frac{3-D+K}{2\mathrm{Pr}}-\frac{D+2}{2\mathrm{Pr}}\right)c^2-\frac{D+2}{2}\left(u^2+\frac{(3-D+K)RT}{\mathrm{Pr}}\right)\right]\boldsymbol{c}\boldsymbol{c}\cdot\nabla(\ln T)d\boldsymbol{\xi}=\frac{(D+2)R}{\mathrm{Pr}}p\nabla T. \tag{35}$$

In addition, the remaining parts of Eq. (34b) are equal to $4p\boldsymbol{u}[\boldsymbol{S}-\vartheta\boldsymbol{I}/(K+3)]=2\boldsymbol{\sigma}\cdot\boldsymbol{u}/\tau_g$, and their computation demands the 8th-order GHQ accuracy.

To sum up, the requirements, using the specific forms of g^{CE} and h^{CE}, that the 10th-order GHQ accuracy is needed to compute the viscous stress and the 12th-order GHQ accuracy is needed to compute the heat flux far exceed the accuracy of D3V27A7 designed for g. As a result, due to insufficient GHQ accuracy, if Eq. (31) is used to initialize the flow field, then unphysical numerical oscillations may occur, which will be shown in Sec. IV A.

Third, our Chapman-Enskog-expansion–based lifting relation is derived from the original exponential equilibria Eq. (11), while the exponential equilibria are replaced by the truncated Hermite polynomials Eq. (30) during the LBM or DUGKS simulations. In other words, the Chapman-Enskog-expansion–based lifting relations, Eq. (31), are only appropriate from the theoretical viewpoint only. Next, we shall prove that the Hermite-expansion–based lifting relations can in fact be derived from Eq. (31), as shown in the following subsection.

C. The Chapman-Enskog analysis based on the truncated Hermite-polynomial equilibria

This subsection is divided into three parts. In the first part, we shall show that the Hermite-expansion–based lifting relations in Eq. (28) can be acquired by the CE analysis based on the truncated Hermite-polynomial equilibria of $g^{\mathrm{eq},(3)}$ and $h^{\mathrm{eq},(2)}$. Compared with the determination of the nonequilibrium Hermite polynomial distributions in the Boltzmann-BGK equation [22,26], we here extend this manipulation to analyze the reduced distributions in the total-energy DDF model. Then in the second part,

we discuss the relation between the order of CE expansions and the truncated order of Hermite equilibria. If the operator $D_t = (\partial_t + \boldsymbol{\xi}\cdot\boldsymbol{\nabla} + \boldsymbol{b}\cdot\boldsymbol{\nabla}_{\boldsymbol{\xi}})$ applies to either the original exponential or the truncated Hermite-polynomial equilibria, then the power exponent in particle velocity (i.e., m in ξ^m) will increase by one. For an Nth truncated Hermite-polynomial equilibrium, however, only the first $(N-M+1)$ Hermite coefficients are correctly derived from the $O(\tau^M)$ CE approximation. This observation is also reported in Shan *et al.* [22] without an explicit proof. Here we shall rigorously prove such a conclusion by the *fundamental theorem of linear maps*. In the third part, we examine the relationship between the number of Hermite coefficients necessary to recover a macroscopic system and the order of the Hermite-polynomial equilibrium. As a result, given a system with many equations and timescales, an inequality for the required order of a Hermite-polynomial equilibrium is developed.

First, we examine the CE expansions based on $g^{\mathrm{eq},(3)}$ and $h^{\mathrm{eq},(2)}$. Without lose of generality, we consider an arbitrary function $f(\boldsymbol{x},\boldsymbol{\xi},t)$ with its Nth-order Hermite polynomial given by

$$f^{(N)}(\boldsymbol{x},\boldsymbol{\xi},t) = \omega(\boldsymbol{\xi},T_0)\sum_{k=0}^{N}\frac{1}{k!}a_{\boldsymbol{i}}^{(k)}(\boldsymbol{x},t,T_0)\mathcal{H}_{\boldsymbol{i}}^{(k)}(\boldsymbol{\xi},T_0) = \omega(\boldsymbol{\xi},T_0)\sum_{k=0}^{N}\frac{1}{k!}a_{i_1\cdots i_k}^{(k)}(\boldsymbol{x},t,T_0)\mathcal{H}_{i_1\cdots i_k}^{(k)}(\boldsymbol{\xi},T_0), \tag{36}$$

where $\mathcal{H}_{\boldsymbol{i}}^{(k)}(\boldsymbol{\xi},T_0)$ is the kth-order Hermite polynomial (see Appendix D). We apply the operator $D_t = (\partial_t + \boldsymbol{\xi}\cdot\boldsymbol{\nabla} + \boldsymbol{b}\cdot\boldsymbol{\nabla}_{\boldsymbol{\xi}})$ to it and obtain

$$\begin{aligned}
D_t f^{(N)}(\boldsymbol{x},\boldsymbol{\xi},t) &= \omega\sum_{k=0}^{N}\frac{1}{k!}\left[\left(\partial_t a_{i_1\cdots i_k}^{(k)} + \xi_i\nabla_i a_{i_1\cdots i_k}^{(k)}\right)\mathcal{H}_{i_1\cdots i_k}^{(k)} - \frac{b_i a_{i_1\cdots i_k}^{(k)}}{\sqrt{RT_0}}\mathcal{H}_{ii_1\cdots i_k}^{(k+1)}\right]\\
&= \omega\sum_{k=0}^{N}\frac{1}{k!}\left[\partial_t a_{i_1\cdots i_k}^{(k)}\mathcal{H}_{i_1\cdots i_k}^{(k)} + \sqrt{RT_0}\left(\nabla_i a_{i_1\cdots i_k}^{(k)}\mathcal{H}_{ii_1i_2\cdots i_k}^{(k+1)} + \sum_{j=1}^{k}\nabla_j a_{i_1\cdots i_k}^{(k)}\mathcal{H}_{i_1i_2\cdots i_{j-1}i_{j+1}\cdots i_k}^{(k-1)}\right) - \frac{b_i a_{i_1\cdots i_k}^{(k)}}{\sqrt{RT_0}}\mathcal{H}_{ii_1\cdots i_k}^{(k+1)}\right]\\
&= \omega\left[\begin{array}{l}\partial_t a^{(0)} + \sqrt{RT_0}\nabla_i a_i^{(1)} + \displaystyle\sum_{k=1}^{N-1}\frac{\partial_t a_{i_1\cdots i_k}^{(k)} + \sqrt{RT_0}\nabla_{i_{k+1}}a_{i_1\cdots i_{k+1}}^{(k+1)} + k\left(\sqrt{RT_0}\nabla_{i_k} - b_{i_k}/\sqrt{RT_0}\right)a_{i_1\cdots i_{k-1}}^{(k-1)}}{k!}\mathcal{H}_{i_1\cdots i_k}^{(k)}\\ + \dfrac{\partial_t a_{i_1\cdots i_N}^{(N)} + N\left(\sqrt{RT_0}\nabla_{i_N} - b_{i_N}/\sqrt{RT_0}\right)a_{i_1\cdots i_{N-1}}^{(N-1)}}{N!}\mathcal{H}_{i_1\cdots i_N}^{(N)} + \dfrac{\left(\sqrt{RT_0}\nabla_{i_{N+1}} - b_{i_{N+1}}/\sqrt{RT_0}\right)a_{i_1\cdots i_N}^{(N)}}{N!}\mathcal{H}_{i_1\cdots i_{N+1}}^{(N+1)}\end{array}\right],
\end{aligned} \tag{37}$$

where the deriviation relies on the tensor symmetry property of Hermite polynomials. From Eqs. (26) and (27), the Hermite coefficients for the equilibria in Grad's short-hand notation [27] are computed as

$$\tilde{a}^{(0)}(g^{\mathrm{eq},(3)}) = \rho,\quad \tilde{\boldsymbol{a}}^{(1)}(g^{\mathrm{eq},(3)}) = \rho\frac{\boldsymbol{u}}{\sqrt{RT_0}},\quad \tilde{\boldsymbol{a}}^{(2)}(g^{\mathrm{eq},(3)}) = \rho\left[\frac{\boldsymbol{u}^2}{RT_0} + \left(\frac{T}{T_0}-1\right)\boldsymbol{I}\right], \tag{38a}$$

$$\tilde{\boldsymbol{a}}^{(3)}(g^{\mathrm{eq},(3)}) = \rho\left[\frac{\boldsymbol{u}^3}{(RT_0)^{3/2}} + \left(\frac{T}{T_0}-1\right)\frac{\boldsymbol{uI}}{\sqrt{RT_0}}\right],\quad \tilde{\boldsymbol{a}}^{(n\geqslant 4)}(g^{\mathrm{eq},(3)}) = \boldsymbol{0},\quad \tilde{a}^{(0)}(h^{\mathrm{eq},(2)}) = \rho E, \tag{38b}$$

$$\tilde{\boldsymbol{a}}^{(1)}(h^{\mathrm{eq},(2)}) = (\rho E + p)\frac{\boldsymbol{u}}{\sqrt{RT_0}},\quad \tilde{\boldsymbol{a}}^{(2)}(h^{\mathrm{eq},(2)}) = \rho E\left[\frac{\boldsymbol{u}^2}{RT_0} + \left(\frac{T}{T_0}-1\right)\boldsymbol{I}\right] + \frac{T}{T_0}\left(2\rho\boldsymbol{u}^2 + p\boldsymbol{I}\right),\quad \tilde{\boldsymbol{a}}^{(n\geqslant 3)}(h^{\mathrm{eq},(2)}) = \boldsymbol{0}. \tag{38c}$$

Applying the similar manipulation in Shan *et al.* [22] to here Guo *et al.*'s total-energy DDF model, the Hermite expansion coefficients for $D_t g^{\mathrm{eq},(3)}$ and $D_t h^{\mathrm{eq},(2)}$, up to the order of $O(\tau^0)$, in Grad's short-hand notation can be explicitly expressed as

$$\tilde{a}^{(0)}(D_t g^{\mathrm{eq},(3)}) = 0,\quad \tilde{\boldsymbol{a}}^{(1)}(D_t g^{\mathrm{eq},(3)}) = \boldsymbol{0},\quad \tilde{\boldsymbol{a}}^{(2)}(D_t g^{\mathrm{eq},(3)}) = \rho\frac{T}{T_0}\left[\boldsymbol{\nabla u} + (\boldsymbol{\nabla u})^T - \frac{2}{K+3}\vartheta\boldsymbol{I}\right], \tag{39a}$$

$$\tilde{\boldsymbol{a}}^{(3)}(D_t g^{\mathrm{eq},(3)}) = \frac{1}{\sqrt{RT_0}}\left\{\left(2\boldsymbol{I} - \frac{T}{T_0} - \frac{\boldsymbol{u}^2}{RT_0}\right)\boldsymbol{\nabla}p + \boldsymbol{\nabla}\cdot\left(\rho\boldsymbol{u}^2\boldsymbol{I}\right) - RT_0\boldsymbol{I}\boldsymbol{\nabla}\rho - \nabla_i\left[\left(\rho\boldsymbol{u}^2 + p\boldsymbol{I}\right)\boldsymbol{u}u_i\right] - \frac{2p\vartheta\boldsymbol{uI}}{(K+3)RT_0}\right\}, \tag{39b}$$

$$\tilde{\boldsymbol{a}}_i^{(4)}(D_t g^{\mathrm{eq},(3)}) = \frac{4\rho(RT_0\nabla_i - b_i)}{\sqrt{RT_0}}\left[\frac{\boldsymbol{u}^3}{(RT_0)^{3/2}} + \left(\frac{T}{T_0}-1\right)\frac{\boldsymbol{uI}}{\sqrt{RT_0}}\right],\quad \tilde{\boldsymbol{a}}^{(n\geqslant 5)}(D_t g^{\mathrm{eq},(3)}) = \boldsymbol{0}, \tag{39c}$$

$$\begin{aligned}
\tilde{a}^{(0)}(D_t h^{\mathrm{eq},(2)}) &= \rho\boldsymbol{u}\cdot\boldsymbol{b},\quad \tilde{a}_i^{(1)}(D_t h^{\mathrm{eq},(2)})\\
&= \frac{1}{\sqrt{RT_0}}\left\{\rho u_i u_j b_j + (p-\rho E)b_i + \frac{K+5}{2}pR\nabla_i T + \frac{2K+4}{K+3}pu_i\vartheta + 2u_i u_j\nabla_j p + 2pu_j\nabla_i u_j\right\},
\end{aligned} \tag{39d}$$

$$\tilde{\boldsymbol{a}}^{(2)}(D_t h^{\mathrm{eq},(2)}) = \frac{1}{RT_0}\left\{\begin{aligned}&(\rho\boldsymbol{u}^2 + p\boldsymbol{I})u_k(b_k - \nabla_k E) - \left[3\boldsymbol{u}^2 + \frac{u^2 + (K+1)RT}{2}\boldsymbol{I}\right]u_k\nabla_k p\\ &- \frac{u^2 + (K+7)RT}{2}\left(\boldsymbol{u}\nabla p + \rho u_i u_k \nabla_k u_j + \rho u_j u_k \nabla_k u_i\right)\\ &+ p\boldsymbol{u}\boldsymbol{b} - \frac{\gamma u^2 + (K+3)RT}{2}p\vartheta\boldsymbol{I} - \boldsymbol{u}^2\left[Eu_k\nabla_k\rho + \vartheta\frac{\rho u^2 + (K+5+4\gamma)p}{2}\right]\end{aligned}\right\}$$
$$- \frac{\boldsymbol{I}}{T_0}\left[\frac{K+7}{K+3}pT\vartheta + u_k\nabla_k(pT)\right] + \boldsymbol{I}\left[\frac{\rho u^2 + (K+5)p}{2}\vartheta - \rho u_k b_k + u_k\nabla_k(p+\rho E)\right] + 2\nabla_i((p+\rho E)u_j), \tag{39e}$$

$$\tilde{\boldsymbol{a}}^{(3)}(D_t h^{\mathrm{eq},(2)}) = \frac{3(RT_0\nabla_i - b_i)}{\sqrt{RT_0}}\left\{\rho E\left[\frac{\boldsymbol{u}^2}{RT_0} + \left(\frac{T}{T_0} - 1\right)\boldsymbol{I}\right] + \frac{T}{T_0}\left(2\rho\boldsymbol{u}^2 + p\boldsymbol{I}\right)\right\},\quad \tilde{\boldsymbol{a}}^{(n\geqslant 4)}(D_t h^{\mathrm{eq},(2)}) = \boldsymbol{0}. \tag{39f}$$

An interesting observation for Hermite coefficients of $D_t g^{\mathrm{eq},(3)}$ is that the mass conservation, the mass-momentum conservation, and the mass-momentum-energy conservation at the Euler level appear collectively in $\tilde{a}^{(0)}(D_t g^{\mathrm{eq},(3)})$, $\tilde{\boldsymbol{a}}^{(1)}(D_t g^{\mathrm{eq},(3)})$, and $\tilde{\boldsymbol{a}}^{(2)}(D_t g^{\mathrm{eq},(3)})$, respectively. And for $D_t h^{\mathrm{eq},(2)}$, the energy equation and the mass-momentum-energy conservation at the Euler level show up in $\tilde{a}^{(0)}(D_t h^{\mathrm{eq},(2)})$ and $\tilde{\boldsymbol{a}}^{(1)}(D_t h^{\mathrm{eq},(2)})$, respectively. In other words, mass conservation, momentum conservation, and energy equation are three independent components, and at least three Hermite coefficients are required. Moreover, only the second-order Hermite expansion of g and the first-order Hermite expansion of h in the $O(\tau)$ CE approximations are required to recover the NSF system in the total-energy DDF model. g^H in Eq. (28a) can be obtained if we set $\tilde{\boldsymbol{a}}^{(n\geqslant 3)}(D_t g^{\mathrm{eq},(3)})$ to zero. Similarly, h^H in Eq. (28b) can be evaluated through $h^{\mathrm{eq},(2)}$ by keeping only $\tilde{\boldsymbol{a}}^{(n\leqslant 1)}(D_t h^{\mathrm{eq},(2)})$ and $\tilde{\boldsymbol{a}}^{(n\leqslant 1)}(ZD_t g^{\mathrm{eq},(3)})$. By projecting and truncating the Hermite polynomials to a given order finite-dimensional Hilbert space [i.e., a space of $\boldsymbol{\xi}$ spanned by a finite number of Hermite polynomials with the inner product defined as $\langle\phi,\psi\rangle = \int\omega(\xi,T_0)\phi\psi d\boldsymbol{\xi}$], the Hermite-expansion–based lifting relation indeed is the regularization [26] of the CE expansions by filtering out all the higher-order terms.

Second, we shall amend a rigorous proof about the relation between the order of CE approximations and the truncated order of Hermite equilibria, which could be considered as the rationale for neglecting the high-order coefficients. For any square-integrable function $f(\boldsymbol{x},\boldsymbol{\xi},t)$ in the $\boldsymbol{\xi}$ space, i.e.,$f\in\{f|\int f^2 d\boldsymbol{\xi}<\infty\}$, the existence and uniqueness of the Hermite projection, $f(\boldsymbol{x},\boldsymbol{\xi},t)\approx\boldsymbol{A}(\boldsymbol{x},t):\boldsymbol{H}(\boldsymbol{\xi})$, are guaranteed by the completeness and orthogonality of a given set of Hermite polynomials $\boldsymbol{H}(\boldsymbol{\xi})$ [27]. We could consider $\boldsymbol{H}(\boldsymbol{\xi})$ as a set of tensor basis in the $\boldsymbol{\xi}$ space, and $\boldsymbol{A}(\boldsymbol{x},t)$ is the corresponding unique coefficients for a given f. Then we shall discuss the effects of D_t on the set of tensor basis $\boldsymbol{H}(\boldsymbol{\xi})$. The operator $D_t = (\partial_t + \boldsymbol{\xi}\cdot\nabla + \boldsymbol{b}\cdot\nabla_{\boldsymbol{\xi}})$ in Eq. (37) can be viewed as a transformation from the original finite-dimensional subspace V of $\boldsymbol{\xi}$ to a new finite-dimensional subspace W, as

$$\partial_t : V\to W,\quad (\boldsymbol{\xi}\cdot\nabla):V\to W,\quad (\boldsymbol{b}\cdot\nabla_{\boldsymbol{\xi}}):V\to W,\quad \boldsymbol{b}\neq\boldsymbol{0}, \tag{40a}$$

$$f^{\mathrm{eq},(N)}\in V(\boldsymbol{\xi}) = \mathrm{span}\{\mathcal{H}^{(0)}(\boldsymbol{\xi},T_0),\cdots,\mathcal{H}_{\boldsymbol{i}}^{(N)}(\boldsymbol{\xi},T_0)\},\quad \dim(V) = N+1,\quad V\subset W,\quad N\in\mathbb{N}, \tag{40b}$$

$$\partial_t f^{\mathrm{eq},(N)}, \boldsymbol{\xi}\cdot\nabla f^{\mathrm{eq},(N)}, \boldsymbol{b}\cdot\nabla_{\boldsymbol{\xi}} f^{\mathrm{eq},(N)}\in W(\boldsymbol{\xi}) = \mathrm{span}\{\mathcal{H}^{(0)}(\boldsymbol{\xi},T_0),\cdots,\mathcal{H}_{\boldsymbol{i}}^{(N+1)}(\boldsymbol{\xi},T_0)\},\quad \dim(W) = N+2, \tag{40c}$$

where $\mathbb{N}$ is the set of natural number and $\dim(\cdots)$ is the dimension of a given tensor space. From Eq. (37), we can verify that the additivity and homogeneity for the operator D_t, i.e.,

$$\begin{aligned}(\alpha_1\partial_t + \alpha_2\boldsymbol{\xi}\cdot\nabla + \alpha_3\boldsymbol{b}\cdot\nabla_{\boldsymbol{\xi}})(\beta_1 f^{\mathrm{eq},(N)} + \beta_2 g^{\mathrm{eq},(N)}) &= (\alpha_1\partial_t + \alpha_2\boldsymbol{\xi}\cdot\nabla + \alpha_3\boldsymbol{b}\cdot\nabla_{\boldsymbol{\xi}})\beta_1 f^{\mathrm{eq},(N)}\\ &\quad + (\alpha_1\partial_t + \alpha_2\boldsymbol{\xi}\cdot\nabla + \alpha_3\boldsymbol{b}\cdot\nabla_{\boldsymbol{\xi}})\beta_2 g^{\mathrm{eq},(N)}\end{aligned} \tag{41}$$

holds $\forall f^{\mathrm{eq},(N)}, g^{\mathrm{eq},(N)}\in V$, and $\forall\alpha_1,\alpha_2,\alpha_3,\beta_1,\beta_2\in\mathbb{R}$, where $\mathbb{R}$ is the set of real number. Thus, ∂_t, $(\boldsymbol{\xi}\cdot\nabla)$, $(\boldsymbol{b}\cdot\nabla_{\boldsymbol{\xi}})$ are in the set of all the linear maps from V to W denoted as $\mathcal{L}(V,W)$. Also, their ranges and null spaces can be represented in the form of

$$\partial_t f^{\mathrm{eq},(N)}\in\mathrm{range}(\partial_t)\subset W,\quad \mathrm{null}(\partial_t) = \phi,\quad (\boldsymbol{\xi}\cdot\nabla)f^{\mathrm{eq},(N)}\in\mathrm{range}(\boldsymbol{\xi}\cdot\nabla)\subset W,\quad \mathrm{null}(\boldsymbol{\xi}\cdot\nabla) = \phi, \tag{42a}$$

$$\boldsymbol{b}\cdot\nabla_{\boldsymbol{\xi}} f^{\mathrm{eq},(N)}\in\mathrm{range}(\boldsymbol{b}\cdot\nabla_{\boldsymbol{\xi}})\subset W,\quad \mathrm{null}(\boldsymbol{b}\cdot\nabla_{\boldsymbol{\xi}}) = \mathrm{span}\{\mathcal{H}^{(0)}(\boldsymbol{\xi},T_0)\}\subset V,\quad \boldsymbol{b}\neq\boldsymbol{0}, \tag{42b}$$

where ϕ is the empty set. According to the *fundamental theorem of linear maps*, the range of ∂_t, $(\boldsymbol{\xi}\cdot\nabla)$, $(\boldsymbol{b}\cdot\nabla_{\boldsymbol{\xi}})\in\mathcal{L}(V,W)$ can be evaluated by

$$\dim[\mathrm{range}(\partial_t)] = \dim(V) - \dim(\mathrm{null}(\partial_t)) = N+1,\quad \mathrm{range}(\partial_t) = \mathrm{span}\{\mathcal{H}^{(0)}(\boldsymbol{\xi},T_0),\cdots,\mathcal{H}_{\boldsymbol{i}}^{(N)}(\boldsymbol{\xi},T_0)\}, \tag{43a}$$

$$\dim[\mathrm{range}(\boldsymbol{\xi}\cdot\nabla)] = N+1,\quad \mathrm{range}(\boldsymbol{\xi}\cdot\nabla) = \mathrm{span}\left\{\mathcal{H}_i^{(1)}, \mathcal{H}^{(0)}\delta_{ij} + \mathcal{H}_{ij}^{(2)}, 2\mathcal{H}_i^{(1)}\delta_{jk} + \mathcal{H}_{ijk}^{(3)},\cdots, N\mathcal{H}_{i_1\cdots i_{N-1}}^{(N-1)}\delta_{i_N i_{N+1}} + \mathcal{H}_{i_1\cdots i_{N+1}}^{(N+1)}\right\}, \tag{43b}$$

$$\dim[\mathrm{range}(\boldsymbol{b}\cdot\nabla_{\boldsymbol{\xi}})] = \dim(V) - \dim[\mathrm{null}(\boldsymbol{b}\cdot\nabla_{\boldsymbol{\xi}})] = N,\quad \mathrm{range}(\boldsymbol{b}\cdot\nabla_{\boldsymbol{\xi}}) = \mathrm{span}\{\mathcal{H}^{(0)}(\boldsymbol{\xi},T_0),\cdots,\mathcal{H}_{\boldsymbol{i}}^{(N-1)}(\boldsymbol{\xi},T_0)\},\quad \boldsymbol{b}\neq\boldsymbol{0}. \tag{43c}$$

From Eq. (43b), the nth-order ($1 \leqslant n \leqslant N-1$) Hermite coefficient of $\boldsymbol{\xi}\cdot\nabla f^{\mathrm{eq}}$ depends on the $(n-1)$-th-order and the $(n+1)$-th-order coefficients of f^{eq}. Hence, if f^{eq} is truncated to the Nth order, then only the Nth-order Hermite coefficient of $\boldsymbol{\xi}\cdot\nabla f^{\mathrm{eq},(N)}$ is incomplete, which cannot reflect any conservative law. In conclusion, the Nth Hermite order of $f^{\mathrm{eq},(N)}$ corresponds to $(N-1)$-th valid Hermite order of $D_t f^{\mathrm{eq},(N)}$. Therefore, the Nth and higher-order Hermite coefficients of $D_t f^{\mathrm{eq},(N)}$ in Eq. (37) are all incomplete or spurious. It follows that $\tilde{\boldsymbol{a}}^{(3)}(D_t g^{\mathrm{eq},(3)})$, $\tilde{\boldsymbol{a}}^{(4)}(D_t g^{\mathrm{eq},(3)})$, $\tilde{\boldsymbol{a}}^{(2)}(D_t h^{\mathrm{eq},(2)})$, and $\tilde{\boldsymbol{a}}^{(3)}(D_t h^{\mathrm{eq},(2)})$ are all inappropriately represented and should be eliminated since they have no impact on the resulting NSF system but may induce numerical errors.

Third, we can infer the required order of the Hermite-polynomial equilibrium when recovering a macroscopic system. From the aforementioned discussion, the order of the Hermite polynomial equilibrium N must satisfy the inequality as

$$N \geqslant N_{\mathrm{mac}} + N_{\mathrm{CE}} - 1, \tag{44}$$

where N_{mac} is the number of the Hermite expansion coefficients involved in a macroscopic system, and N_{CE} represents the order of the CE approximation, implying that the number of timescales is $(N_{\mathrm{CE}}+1)$. For instance, $f^{\mathrm{eq},(N)}$ requires a Hermite expansion with $N \geqslant 2$ or at least $(2N)$ or fourth-order GHQ accuracy to produce the Euler equation from three Hermite coefficients (or $N_{\mathrm{mac}}=3$) of f with order $O(1)$ (or $N_{\mathrm{CE}}=0$), which involves one timescale and three separate moment equations. Two moment equations and two timescales (or $N_{\mathrm{CE}}=1$) are included in the athermal Navier-Stokes equation. The first three Hermite coefficients (or $N_{\mathrm{mac}}=3$) of f are utilized to recover the athermal Navier-Stokes equation, particularly the viscous stress in the equations, hence $f^{\mathrm{eq},(N)}$ needs a Hermite expansion with $N \geqslant 3$ or at least sixth-order GHQ accuracy. Three moment equations and two timescales (or $N_{\mathrm{CE}}=1$) are incorporated in the thermal compressible NSF equation. The first four Hermite coefficients (or $N_{\mathrm{mac}}=4$) of f are applied to derive the thermal compressible NSF equation, especially the heat flux in the equations, consequently $f^{\mathrm{eq},(N)}$ demands a Hermite expansion with $N \geqslant 4$ or at least eighth-order GHQ accuracy. We note that this inference does not conflict with our previous efficient DUGKS method for a compressible flow [19,20]. Under the total-energy DDF formulation, however, the mass-momentum equation with the viscous stress is obtained by the first three Hermite coefficients (or $N_{\mathrm{CE}}=3$) of the first reduced distribution function, and the energy equation with the heat flux is derived by the first two Hermite coefficients (or $N_{\mathrm{CE}}=2$) of the second reduced distribution function. Therefore, as shown in Table I, the equilibrium of the first reduced distribution function requires a Hermite expansion with $N \geqslant 3$ or at least sixth-order GHQ accuracy, and the equilibrium of the second reduced distribution function demands a Hermite expansion with $N \geqslant 2$ or at least fourth-order GHQ accuracy.

IV. THREE-DIMENSIONAL TAYLOR-GREEN VORTEX PROBLEM

The main objective here is to demonstrate the use of the two sets of lifting relations in the initialization of compressible flow simulations. The DUGKS approach using the total energy DDF model, as discussed in Sec. II, is used as the numerical method. The 3D Taylor-Green vortex flow is used as the macroscopic initial condition. The computation domain $[0,2\pi L]\times[0,2\pi L]\times[0,2\pi L]$ is discretized by a uniform grid and the periodic boundary condition is applied in all three Cartesian directions. The sixth-order TENO scheme [23] is incorporated in our simulations.

The initial pressure p and velocity $\boldsymbol{u}=(u,v,w)$ are specified as

$$\begin{aligned}
p(\boldsymbol{x},t=0) &= p_0 + \frac{\rho u_0^2}{16}\left[\cos\left(\frac{2x}{L}\right)+\cos\left(\frac{2y}{L}\right)\right] \\
&\quad\times\left[\cos\left(\frac{2z}{L}\right)+2\right], \\
u(\boldsymbol{x},t=0) &= u_0\sin\left(\frac{x}{L}\right)\cos\left(\frac{y}{L}\right)\cos\left(\frac{z}{L}\right), \\
v(\boldsymbol{x},t=0) &= -u_0\cos\left(\frac{x}{L}\right)\sin\left(\frac{y}{L}\right)\cos\left(\frac{z}{L}\right), \\
w(\boldsymbol{x},t=0) &= 0,
\end{aligned} \tag{45}$$

where the variables with subscript "0" represent the constant reference values and $p_0=\rho_0 RT_0$.

Two initial conditions for density and temperature will be studied. The first case is uniform density $\rho=\rho_0$ and nonuniform temperature $T=p/(\rho_0 R)$ at $t=0$, which is discussed in Sec. IV A. The second case is uniform temperature $T=T_0$ and nonuniform density $\rho=p/(RT_0)$ at $t=0$, presented in Sec. IV B. The initial Mach and Reynolds numbers are defined by $\mathrm{Ma}=u_0/\sqrt{\gamma RT_0}$ and $\mathrm{Re}=\rho_0 u_0 L/\mu_0$, respectively. We set $D=3$, $K=2$, $R=0.5$, $L=1$, $u_0=1$, $\rho_0=1$, and $\mathrm{Re}=1600$ for both cases. For the cases in Sec. IV A, we take $T_0=1000/7$, $\mathrm{Ma}=0.1$, $\mathrm{Pr}=1$, and $\mathrm{CFL}=0.75$. For the cases in Sec. IV B, we take $T_0=10/7$, $\mathrm{Ma}=1.0$, $\mathrm{Pr}=0.71$, and $\mathrm{CFL}=0.5$. Furthermore, the previous study [20] simulated the cases at $\mathrm{Ma}=1.25$ on a 256^3 mesh with the same discrete velocity model and applied the van Leer limiter [28] and a fifth-order weighted essentially nonoscillatory (WENO) scheme [29] for reconstructions, respectively. While the simulation using the van Leer limiter was stable, the one with the WENO scheme was not. Here, our simulation using the TENO scheme is numerically unstable at $\mathrm{Ma}=1.25$. This is because the numerical stability of the kinetic model at high Mach numbers is weakened by the reduced numerical viscosity of a high-order reconstruction scheme, and more research is required to create a robust DUGKS for compressible turbulence. To further test the lifting relations, we also consider an alternative kinetic model, Qi *et al.*'s total energy DDF model (see Appendix B), in Sec. IV B.

The Taylor-Green vortex problem was introduced Taylor and Green [30] to illustrate the formation of small-scale flow structures due to nonlinear advection, and subsequent transition of the laminar flow to turbulence of an incompressible fluid. Here the same initial flow is used but the NSF system for a general compressible flow is solved. In the simulations, we will focus on the evolution of the statistics including the total kinetic energy K_ρ, the solenoidal dissipation ε_s, the compressive dissipation ε_c, and the total dissipation ε, which are

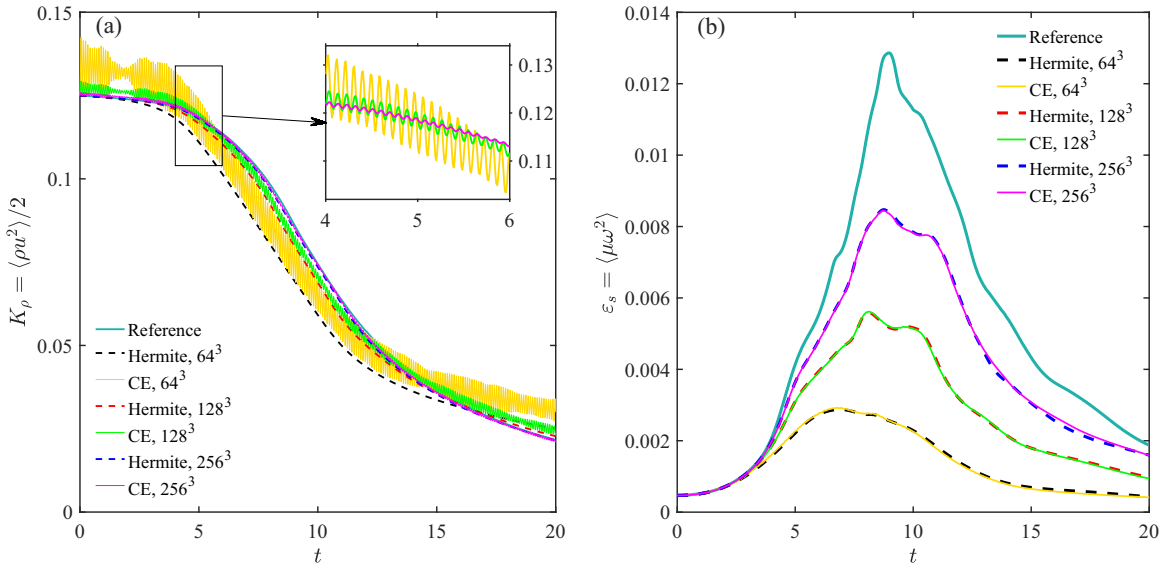

FIG. 1. Temporal evolution of (a) total kinetic energy K_ρ with a zoom-in view of the oscillations inserted and (b) solenoidal dissipation ε_s for the case of Ma $= 0.1$. The reference data are taken from Ref. [31] obtained by the pseudospectral method on a 512^3 mesh.

defined as

$$K_\rho = \frac{1}{2}\langle \rho \boldsymbol{u} \cdot \boldsymbol{u} \rangle, \quad \varepsilon_s = \left\langle \frac{D-1}{2} \mu \omega^2 \right\rangle,$$
$$\varepsilon_c = \left\langle \left(\mu_V + \frac{2(D-1)}{D} \mu \right) \vartheta^2 \right\rangle, \varepsilon = \varepsilon_s + \varepsilon_c, \qquad (46)$$

where $\langle \cdots \rangle$ denotes the spatial average over the flow domain at a given time, and the ε_c can be neglected for the case in Sec. IV A since Ma $= 0.1$.

A. The case with uniform initial density and nonuniform initial temperature

We first test both sets of lifting relations as the initialization method, for an initial flow with a uniform density but a nonuniform temperature. The idea is to demonstrate the numerical errors caused by inadequate GHQ accuracy in the Chapman-Enskog-expansion–based lifting relations, Eq. (31). Here $\rho = \rho_0$ and $T = p/(\rho_0 R)$ at $t = 0$, so the initial temperature field is nonuniform.

The time evolutions of total kinetic energy and solenoidal dissipation are presented in Fig. 1. Since the initial Mach number (Ma $= 0.1$) is small, the flow field can be regarded as incompressible flow. Our results are compared to the reference data obtained by the pseudospectral method using a 512^3 grid resolution [31].

For the Hermite-expansion–based lifting relation, the total kinetic energy [in Fig. 1(a)] is underestimated for the interval of $0 < t < 16.5$ and overestimated for $t > 16.5$ at the two low grid resolutions (64^3 and 128^3). And the solenoidal dissipation [in Fig. 1(b)] is underestimated for all cases, compared to the spectral result, when small-scale structures have developed. At low grid resolutions, the physical dissipation is underestimated due to the fact that small-scale features cannot be resolved. At the same time, the numerical dissipation in DUGKS associated with interpolations is large. The fact that the kinetic energy is underestimated implies that the numerical dissipation dominates when compared to the errors due to insufficient grid resolution. When the grid resolution increases to 256^3, the kinetic energy is reasonably predicted with the initialization done by the Hermite-expansion–based lifting relations, indicating that the numerical dissipation essentially balances the unresolved physical dissipation, making the numerical method a good implicit large-eddy simulation tool. Additional simulations using DUGKS with the van-Leer limiter [28] for reconstructions are performed and the results (not shown here) show that the high-order reconstruction methods like the sixth-order TENO scheme can improve the results at coarse resolutions even for the nearly incompressible flow considered here.

Next, we consider the cases with the flow initialization done by the Chapman-Enskog-expansion–based lifting relation. The total kinetic energy is overestimated for $0 < t < 5$ and $t > 14$ but underestimate for $5 < t < 14$ at the two low grid resolutions (64^3 and 128^3). The most obvious difference is the high-frequency, unphysical noises in the total kinetic energy in Fig. 1(a). The oscillations are visible in all three resolutions, and their magnitudes remain similar even the kinetic energy is decayed significantly.

Here we develop a theory for predicting the oscillations of the total kinetic energy ascribed to the numerical errors in the initialization. We first note that the acoustic timescale, which is significantly shorter than the typical advection timescale in the NSF system, is where the numerical disturbances are originated. Additionally, the numerical disturbances in the weakly compressible flows are confined to a fluid particle's location and a small area around it, leading to a different space scale compared with the NSF system. Regarding the distinctions between our study and linear stability analyses like the Squire theorem [32], two points can be made. First, the disturbances in the linear stability analyses, which are small quantities whose squares may be neglected, share the same time and space scales with the NSF system. The disturbances in our study, however, are not only small quantities but also have

completely different time and space scales from those in the NSF system. The flows determined by the NSF system may appear stationary relative to acoustic waves. Second, since Ma = 0.1, we utilize an inviscid and barotropic fluid model [33] here, and the disturbances in the linear stability analyses are consistent with the equations in the NSF system. In our study, the Euler equations for barotropic fluid without external force, which describe the evolution of the disturbances, are written in the form of

$$\partial_t \rho' + \nabla \cdot (\rho' \boldsymbol{u}') = 0, \tag{47a}$$

$$\partial_t (\rho' \boldsymbol{u}') + \nabla \cdot (\rho' \boldsymbol{u}' \boldsymbol{u}' + p') = \boldsymbol{0}, \tag{47b}$$

$$dp'/d\rho' = c_s^2, \tag{47c}$$

where ρ' is the disturbed density, $\boldsymbol{u}' = (u', v', w')$ is the disturbed velocity, p' is the disturbed pressure only related to ρ', and $c_s = \sqrt{\gamma R T_0}$ is the speed of sound, which equals to 10 in this case. We can obtain the momentum equation for disturbances, Eq. (47b), in a nonconservation form as

$$\partial_t \boldsymbol{u}' + \boldsymbol{u}' \cdot \nabla \boldsymbol{u}' + c_s^2 \frac{\nabla \rho'}{\rho'} = \boldsymbol{0}, \tag{48}$$

By multiplying $\boldsymbol{u}'$, taking the divergence, and taking the curl to Eq. (48), the equations for disturbed kinetic energy per unit mass, the disturbed dilatation, and the disturbed vorticity, respectively, are given as

$$\partial_t \left(\frac{|\boldsymbol{u}'|^2}{2} \right) + \boldsymbol{u}' \cdot \nabla \left(\frac{|\boldsymbol{u}'|^2}{2} \right) + \boldsymbol{u}' \cdot \frac{c_s^2 \nabla \rho'}{\rho'} = 0, \tag{49a}$$

$$\partial_t \vartheta' + \boldsymbol{u}' \cdot \nabla \vartheta' + \nabla \boldsymbol{u}' : \nabla \boldsymbol{u}' + c_s^2 \nabla \cdot \left(\frac{\nabla \rho'}{\rho'} \right) = 0, \tag{49b}$$

$$\partial_t \boldsymbol{\omega}' + \nabla \times (\boldsymbol{u}' \cdot \nabla \boldsymbol{u}') = \partial_t \boldsymbol{\omega}' + \boldsymbol{u}' \cdot \nabla \boldsymbol{\omega}' - \boldsymbol{\omega}' \cdot \nabla \boldsymbol{u}' + \boldsymbol{\omega}' \vartheta' = \boldsymbol{0}, \tag{49c}$$

where $\vartheta' = \nabla \cdot \boldsymbol{u}'$ is the disturbed dilatation, $\boldsymbol{\omega}' = \nabla \times \boldsymbol{u}'$ is the disturbed vorticity, and $\nabla \boldsymbol{u}' : \nabla \boldsymbol{u}' = \partial_i u_j' \partial_j u_i'$ is the contraction of disturbed velocity gradient $\nabla \boldsymbol{u}'$. Here we apply the surface-deformation tensor $\boldsymbol{B} = \vartheta' \boldsymbol{I} - (\nabla \boldsymbol{u}')^T$ [34], which measures the material rate of change for the surface elements, to simplify the contraction in Eq. (49b) and obtain

$$\partial_t \vartheta' + \boldsymbol{u}' \cdot \nabla \vartheta' = c_s^2 \nabla \cdot \left(\frac{\nabla \rho'}{\rho'} \right) - (\vartheta')^2 + \nabla \cdot (\boldsymbol{B} \cdot \boldsymbol{u}'). \tag{50}$$

By amending the corresponding terms in Eq. (47a), the equation for disturbed kinetic energy per unit volume and disturbed dilatation in conserved forms are given, namely

$$\partial_t \left(\rho' \frac{|\boldsymbol{u}'|^2}{2} \right) + \nabla \cdot \left(\rho' \boldsymbol{u}' \frac{|\boldsymbol{u}'|^2 + 2c_s^2}{2} \right) = c_s^2 \rho' \vartheta', \tag{51a}$$

$$\partial_t (\rho' \vartheta') + \nabla \cdot (\rho' \boldsymbol{u}' \vartheta') = c_s^2 \left(\frac{|\nabla \rho'|^2}{\rho'} - \nabla^2 \rho' \right) - \rho' (\vartheta')^2 + \rho' \nabla \cdot (\boldsymbol{B} \cdot \boldsymbol{u}'), \tag{51b}$$

By taking the spatial average in Eq. (49c), Eq. (51a), and Eq. (51b) for the periodic boundary condition, we can find the equations for the spatial average disturbed vorticity $\langle \boldsymbol{\omega}' \rangle$ and the disturbed total kinetic energy K_ρ' as follows:

$$\partial_t \langle \boldsymbol{\omega}' \rangle = \boldsymbol{0}, \tag{52a}$$

$$\partial_{tt} K_\rho' = \partial_{tt} \left\langle \frac{\rho' |\boldsymbol{u}'|^2}{2} \right\rangle = c_s^4 \left\langle \frac{|\nabla \rho'|^2}{\rho'} \right\rangle - c_s^2 \langle \rho' (\vartheta')^2 \rangle + c_s^2 \langle \rho' \nabla \cdot (\boldsymbol{B} \cdot \boldsymbol{u}') \rangle. \tag{52b}$$

From Eq. (52a), the spatial average disturbed vorticity is a constant in time. The vorticity associated to the NSF system appears to be stationary compared with the small disturbed vorticity, and the square of the vorticity can be approximated by

$$\langle |\boldsymbol{\omega} + \boldsymbol{\omega}'|^2 \rangle = \langle \omega^2 \rangle + 2 \langle \boldsymbol{\omega} \rangle \cdot \langle \boldsymbol{\omega}' \rangle \approx \langle \omega^2 \rangle.$$

As a result, the disturbed vorticity almost has no contributions to the solenoidal dissipation. The comparison in Fig. 1(b) confirms that the noises seen in the kinetic energy do not seem to appear in the simulated solenoidal dissipation.

For the disturbed total kinetic energy, the right-hand-side terms of its oscillation equation, Eq. (52b), represent the vibrations related to the nonuniform disturbed density, the material rate of change for the volume elements, and the material rate of change for the surface elements, respectively. The last two terms can be ignored since the material rates of change for the volume elements and the surface elements are very small in this case with Ma = 0.1. Since the oscillations in Fig. 1(a) have essentially the same period roughly equal to 0.1, the disturbed density can be assumed to have the form of a traveling wave with a phase speed of c_s, i.e.,

$$\rho'(\boldsymbol{x}, t) = A_0 \sin \varphi, \quad \varphi = \boldsymbol{k} \cdot \left(\boldsymbol{x} - \frac{\boldsymbol{k}}{|\boldsymbol{k}|} c_s t \right) + \varphi_0, \tag{53}$$

TABLE II. The total kinetic energy K_ρ and its oscillation amplitude in the cases with Chapman-Enskog-expansion–based lifting relations.

Case	Maximum total kinetic energy $(K_\rho)_{\max}$	Maximum oscillation amplitude $(K_\rho)_{\max} - K_\rho(t=0)$	Normalized maximum oscillation amplitude $(K_\rho)_{\max}/K_\rho(t=0) - 1$
64^3	0.142386	0.017386	0.139088
128^3	0.129322	0.004322	0.034576
256^3	0.125994	0.000994	0.007952

where A_0 is the amplitude, $\boldsymbol{k}$ is the constant wave vector, and φ_0 is the initial phase. By changing the integral variables of the spatial average $\langle\cdots\rangle$, the nonuniform disturbed density term in Eq. (52b) can be evaluated by

$$\frac{|\nabla\rho'|^2}{\rho'} = A_0|\boldsymbol{k}|^2\frac{\cos^2\varphi}{\sin\varphi},\quad \left\langle\frac{|\nabla\rho'|^2}{\rho'}\right\rangle = \frac{A_0|\boldsymbol{k}|^2}{\varphi_{\max}-\varphi_{\min}}\left(\int_{\varphi_{\min}}^{\varphi_{\max}}\frac{\cos^2\varphi}{\sin\varphi}d\varphi\right) = \frac{A_0|\boldsymbol{k}|^2}{\varphi_{\max}-\varphi_{\min}}\left[\ln\left(\tan\left(\frac{\varphi}{2}\right)\right)+\cos\varphi\right]_{\varphi_{\min}}^{\varphi_{\max}}, \tag{54}$$

where $\varphi_{\min}$ and $\varphi_{\max}$ are the minimum and maximum of φ depending on the wave vector $\boldsymbol{k}$, respectively. By taking the maximum value of $\boldsymbol{k}\cdot\boldsymbol{x}$ in the computation domain as $(\boldsymbol{k}\cdot\boldsymbol{x})_{\max}$, $\varphi_{\min}$ and $\varphi_{\max}$ are specified as

$$\varphi_{\min} = -(\boldsymbol{k}\cdot\boldsymbol{x})_{\max} - |\boldsymbol{k}|c_s t + \varphi_0,\quad \varphi_{\max} = (\boldsymbol{k}\cdot\boldsymbol{x})_{\max} - |\boldsymbol{k}|c_s t + \varphi_0, \tag{55}$$

since φ is a linear function of $\boldsymbol{x}$. With the help of Eq. (55), the spatial average term in Eq. (54) equals to

$$\left\langle\frac{|\nabla\rho'|^2}{\rho'}\right\rangle = \frac{1}{(\boldsymbol{k}\cdot\boldsymbol{x})_{\max}}\ln\left\{1+\frac{2\sin\left[(\boldsymbol{k}\cdot\boldsymbol{x})_{\max}\right]}{\sin\left(|\boldsymbol{k}|c_s t-\varphi_0\right)-\sin\left[(\boldsymbol{k}\cdot\boldsymbol{x})_{\max}\right]}\right\}+\frac{\sin\left[(\boldsymbol{k}\cdot\boldsymbol{x})_{\max}\right]}{(\boldsymbol{k}\cdot\boldsymbol{x})_{\max}}\sin\left(|\boldsymbol{k}|c_s t-\varphi_0\right). \tag{56}$$

The logarithmic term in Eq. (56) may be neglected since it only pertains to nonlinear behaviors and has no effect on the secular numerical oscillations. We yield the periodic solution of the disturbed total kinetic energy K'_ρ in Eq. (52b),

$$K'_\rho(t) = A_0 c_s^2\frac{\sin\left[(\boldsymbol{k}\cdot\boldsymbol{x})_{\max}\right]}{(\boldsymbol{k}\cdot\boldsymbol{x})_{\max}}\sin\left(|\boldsymbol{k}|c_s t-\varphi_0\right). \tag{57}$$

Equation 57 proves that *the total kinetic energy oscillates over time when there are small disturbances in the initial density and velocity brought on by improper initialization.* We note that the aforementioned conclusion holds up on the premise that the disturbances are in the weakly compressible flows with the periodic boundary condition. Due to the shifting of the time and space scales when the Mach number rises in the flows, the disturbances will be coupled with the terms in the NSF system. Therefore, the theory can be expanded to account for the nonphysical oscillations of total kinetic energy in the initial field of all weakly compressible flows with periodic boundary conditions.

When the insufficient GHQ accuracy discrete velocity model, D3V27A7, calculates the nonzero temperature gradient terms in the Chapman-Enskog-expansion–based lifting relations, it causes the disturbances of the initialization associated with the numerical errors. The disturbed velocity $\boldsymbol{u}'$ can be approximated by $\boldsymbol{u}' \sim O(\boldsymbol{u}\Delta x/L)$, where $\Delta x = L/N$ is the mesh size in one direction. The initial velocity $\boldsymbol{u}(t=0)$ has no z-direction component, and as a result, the amplitude A_0 is of the order $O[1/(N^2\mathrm{Ma}^2)]$. For a given Ma, it follows that the maximum oscillation amplitudes of K_ρ with Chapman-Enskog-expansion–based lifting relations scale with $O(1/N^2)$, which are consistent with the data from the three cases, shown in Table II.

The numerical noises may lead to numerical instability in moderate and high Mach number cases. Therefore, the Chapman-Enskog-expansion–based lifting relations may not be suitable for constructing the initial distribution functions with nonzero temperature gradients.

B. The case with uniform initial temperature and nonuniform initial density

Next, the case with uniform initial temperature $T = T_0$ and nonuniform initial density $\rho = p/(RT_0)$ is simulated for Ma = 1.0 in Figs. 2 and 3. In this high-Ma case, our results are compared to the reference data from Ref. [35] where the flow was solved on a 512^3 grid by a finite difference method of the NSF system, combined with the sixth-order TENO scheme with adaptive control of the numerical dissipation. The total kinetic energy in Fig. 2(a) increases with time slightly during $0 < t < 3$ due to the conversion of internal energy to the kinetic energy by the reversible pressure-dilatation transfer as we have discussed previously [19], and then it decays monotonically in time. For the case at 64^3, the kinetic energy is underestimated for $t < 14$ and then overestimated for $t > 14$. As the grid resolution increases, the results converge to the reference data from Ref. [35]. Additionally, two sets of lifting relations yield almost the same results at the same resolution, indicating that the noises in the Chapman-Enskog-expansion–based lifting relations are primarily associated with the temperature gradients in the initial flow rather than the velocity gradients or the dilatation gradients. Interestingly, although D3V27A7 does not meet the formal requirement of the eighth-order accuracy for the Chapman-Enskog-expansion–based lifting relation in the absence of temperature gradients [see Eq. (33a)], this insufficient GHQ accuracy does not cause any problem in the simulated total kinetic energy. We think certain eighth-order terms can still be reasonably calculated by the quadrature of the discrete velocity model even though it lacks the eighth-order accuracy. Furthermore, the velocity gradient tensor $\nabla\boldsymbol{u}$ and the dilatation ϑ of the initial flow are not significant,

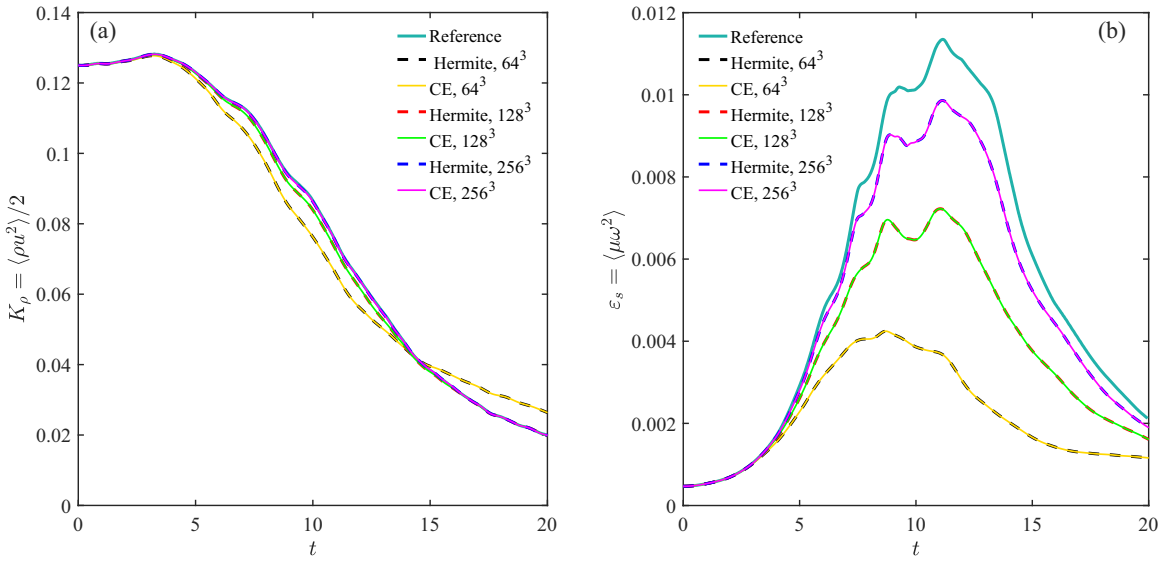

FIG. 2. Temporal evolution of (a) total kinetic energy K_ρ and (b) solenoidal dissipation ε_s for the case of Ma = 1.0. The reference data are taken from Ref. [35] obtained by the sixth-order TENO scheme with adaptive control of the numerical dissipation on a 512^3 mesh.

which implies that the high-order moments of the distribution function are likely small. These may be the reasons for the good simulated total kinetic energy.

At Ma = 1.0, the flow deems to be compressible with the prominent dilatation. We plot the time evolutions of compressive dissipation and total dissipation in Fig. 3. The results based on the two sets of lifting relations overlap, and the peak times are consistent with each other and the reference data. Compared with the solenoid dissipation, the compressive dissipation takes a shorter time to reach its maximum, which is similar to the previous observation in decaying compressible homogeneous isotropic turbulence [19]. This phenomenon indicates that there are at least two timescales in the flow field, and the compressive motion happens rapidly while the vortical structures take a loner time to develop. Furthermore, the maximum compressive dissipation for the case at 256^3 is 1.196 times larger than that from the reference data. We believe that this originates from the difference in the values of the bulk viscosity between our kinetic model and the reference simulation. The bulk viscosity of the reference is zero while the bulk-to-shear viscosity ratio is $\chi = 4/15$ for Guo *et al.*'s model with $K = 2$, and the ratio of $(\mu_V + 4\mu/3)/(4\mu/3) = 1.2$ implied by Eq. (46) explains the observed ratio of 1.196 in Fig. 3. Although the present cases have the different bulk viscosity from the reference, the compressive dissipation is still one to two orders of magnitude smaller than the solenoidal dissipation. Therefore, it is reasonable to compare total kinetic energy, solenoidal dissipation, and total dissipation in the present cases with the reference.

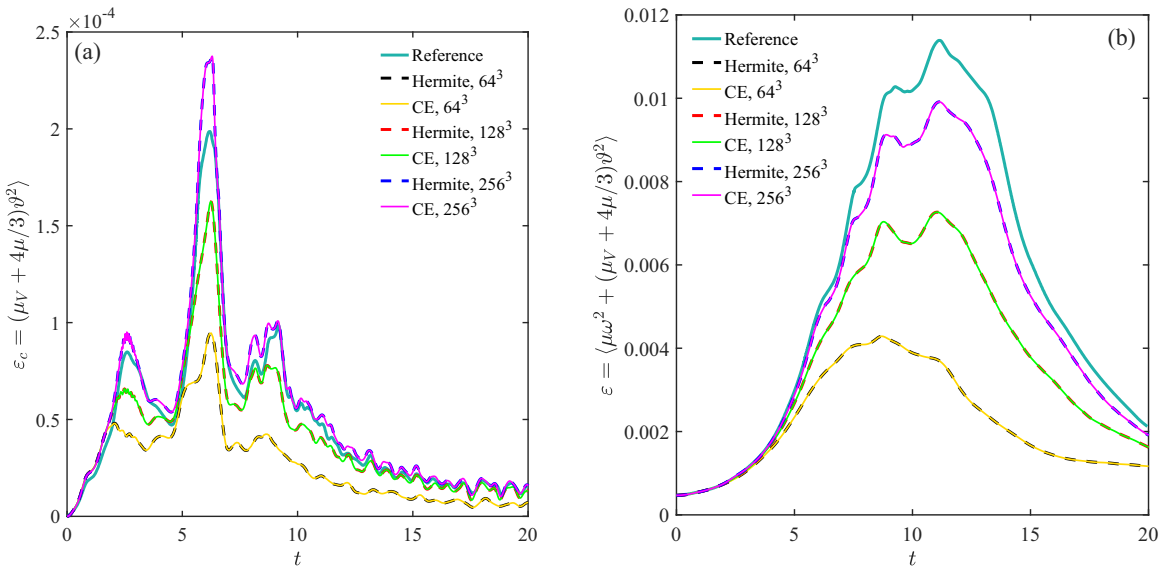

FIG. 3. Temporal evolution of (a) compressive dissipation ε_c and (b) total dissipation ε for the case of Ma = 1.0. The reference data are taken from Ref. [35] obtained by the sixth-order TENO scheme with adaptive control of the numerical dissipation on a 512^3 mesh.

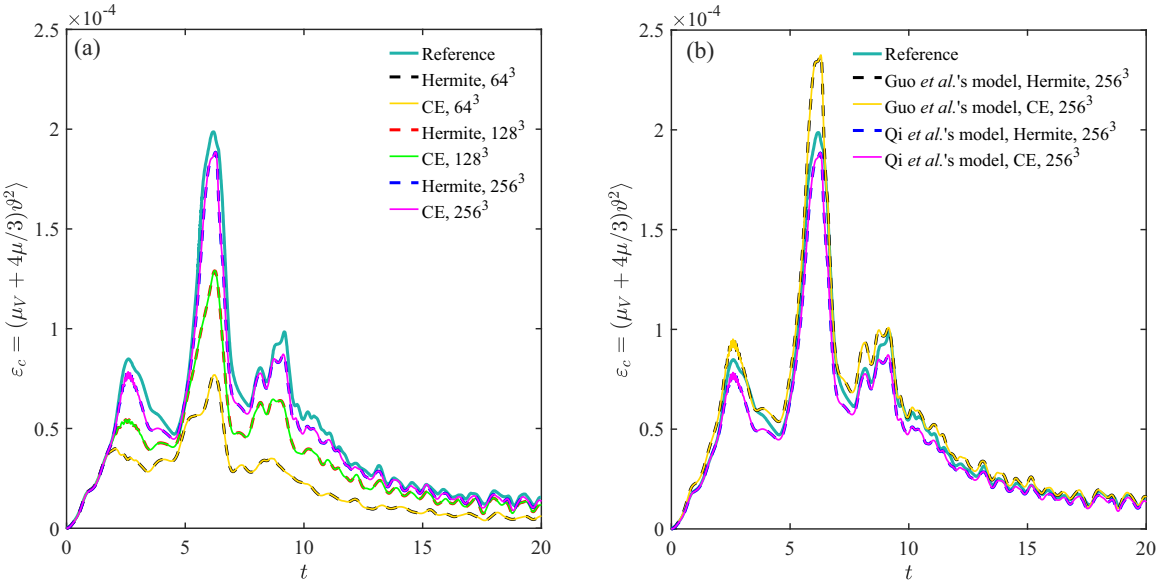

FIG. 4. Temporal evolution of (a) compressive dissipation ε_c for Qi *et al.*'s model [19] and (b) for two alternative kinetic models at the finest resolution for the case of Ma = 1.0. The reference data are taken from Ref. [35] obtained by the sixth-order TENO scheme with adaptive control of the numerical dissipation on a 512^3 mesh.

Finally, numerical simulations for the Ma = 1.0 case and the same initial flow field are also performed using Qi *et al.*'s model with initialization done by the two sets of lifting relations, the results are shown in Appendix B. We purposely set the bulk viscosity to zero in Qi *et al.*'s model, as, in Qi *et al.*'s model, the bulk viscosity can be set to an arbitrary value. Qi *et al.*'s model could be more appropriate when simulating strong compressive effects. Another minor advantage in Qi *et al.*'s model is that the source terms used to adjust the Prandtl number and bulk viscosity has already been expanded in the Hermite space in their design, see the discussions in Appendix B. The results for total kinetic energy, solenoidal dissipation, and total dissipation (not shown) are almost the same as the previous results based on Guo *et al.*'s model, so they are not shown. This confirms that the effects of bulk viscosity on total kinetic energy, solenoidal dissipation, and total dissipation are too weak to be recognized from the flow field. The results of the compressive dissipation based on Qi *et al.*'s model are shown in Fig. 4(a), for three grid resolutions, again the two initialization methods yield identical results. As expected, at the highest resolution, the result of the compressive dissipation based on Qi *et al.*'s model is closer to the reference data, as shown in Fig. 4(b), due to the same null bulk viscosity setting as in the reference.

V. SUMMARY AND CONCLUSIONS

By the $O(\tau)$ CE approximation, we deduce two kinds of lifting relations for the two total-energy DDF models, i.e., the first kind is the Hermite-expansion–based lifting relations based on all the velocity moment constraints implied by the NSF system, and the second kind is the Chapman-Enskog-expansion–based lifting relations using the original exponential equilibria. These lifting relations are intended for fully compressible flows, extending the previous results primarily designed for incompressible flows. While the two kinds are theoretically identical at the level of the NSF system, they are different in numerical implementations due to potential contamination of numerical errors for a given set of particle velocity models (or given GHQ accuracy orders). We analyze the required GHQ accuracy orders for the Chapman-Enskog-expansion–based lifting relations when computing the viscous stress and the heat flux to illustrate the possibility for numerical integration errors in the particle-velocity phase space.

The exponential equilibria are replaced by the Hermite polynomials in LBM or DUGKS, thus we also examine the nonequilibrium distribution based on the CE expansions with the truncated Hermite polynomial equilibria. This procedure illustrates that the Hermite-expansion–based lifting relations can be regarded as the Chapman-Enskog-expansion–based lifting relation in the truncated Hilbert space. Furthermore, we demonstrate that $D_t f^{(N)}$ only has the accurate and complete Hermite coefficients up to the $(N-1)$-th valid Hermite order. We may then infer the minimal order of the corresponding Hermite polynomial equilibria with the required GHQ accuracy for a given multiple-timescale macroscopic system.

Next, we tested the two sets of lifting relations as the initialization tool in numerical simulations for compressible flows, to validate the lifting relations of the first kind, as well as to demonstrate the potential error contamination in the second kind. We perform numerical experiments for subsonic flow and transonic flow using the initial flow from the Taylor-Green vortex problem. Indeed, the potential contamination in the lifting relations of the second kind is confirmed and is reflected as unphysical oscillations in the kinetic energy of the simulated flow. Furthermore, such contamination is closely related to the nonzero temperature gradients in the initial flow. The contamination, however, has essentially no

TABLE III. Three-dimensional discrete velocity models D3V13A5 and D3V27A7. The subscript $_{PP}$ means the parity of the permutation is strictly kept.

Quadrature	Group	$\boldsymbol{\xi}_\alpha$	Number	Weight
D3V13A5	1	$(0, 0, 0)$	1	$2/5$
$r^2 = (5+\sqrt{5})/2$, $s^2 = (5-\sqrt{5})/2$	2	$(r, s, 0)_{PP}$	12	$1/20$
D3V27A7	1	$(0, 0, 0)$	center1	$(720+8\sqrt{15})/2205$
$r^2 = (15+\sqrt{15})/2$	2	$(r, 0, 0)$	center6	$(270-46\sqrt{15})/15435$
$s^2 = 6-\sqrt{15}$	3	$(s, s, 0)$	12	$(162+41\sqrt{15})/6174$
$t^2 = 9+2\sqrt{15}$	4	(t, t, t)	center8	$(783-202\sqrt{15})/24696$

impact on the solenoid dissipation since the oscillations have no contributions to the spatial average of the square of the vorticity. Moreover, the unphysical oscillations in the kinetic energy persist even at high grid resolutions, with the oscillation magnitude decreasing with increasing grid resolution. They also persist in time, so the proper initialization of compressible turbulence is an important issue. In contrast, the Hermite-expansion–based lifting relations are fully consistent with the GHQ accuracy of discrete velocity models and are shown to be a great initialization method. We also tested the two sets of lifting relations as the initialization method for Qi *et al.*'s total energy DDF model capable of arbitrarily adjusting the bulk-to-shear viscosity ratio. Overall, all the results agree well with the reference data at the high grid resolution. In conclusion, the Hermite-expansion–based lifting relations are fully consistent with the model Boltzmann equations and discrete particle velocity models, for compressible flows at all Mach numbers at the level of the NSF system.

Finally, we note that the Hermite-expansion–based lifting relations developed in this work are not just a useful and efficient initialization tool for compressible flows. They are useful in constructing the proper bounce-back boundary conditions [5], coupling the mesoscopic methods with other numerical methods [8,11], formulating a way to accelerate the steady-state flow simulation [36], or extending the theoretical understanding of kinetic methods to general compressible flows.

The data that support the findings of this study are available from the corresponding author upon reasonable request.

Y.Q. thanks Chunyou Liu and Wenjuan Zheng for many useful discussions. This work has been supported by the National Natural Science Foundation of China (NSFC Awards No. T2250710183, No. U2241269, No. 91852205, No. 11961131006, No. 42075071, and No. 91741101), NSFC Basic Science Center Program (Award No. 11988102), the Taizhou-Shenzhen Innovation Center, Guangdong Provincial Key Laboratory of Turbulence Research and Applications (Grant No. 2023B1212060001), Guangdong-Hong Kong-Macao Joint Laboratory for Data-Driven Fluid Mechanics and Engineering Applications (2020B1212030001), and Shenzhen Science & Technology Program (Grant No. KQTD20180411143441009, 2020-148). Computing resources are provided by the Center for Computational Science and Engineering of Southern University of Science and Technology.

APPENDIX A: DISCRETE PARTICLE VELOCITY MODELS: D3V27A7 AND D3V13A5

DUGKS is an *off-lattice* method, namely the discrete particle velocities are decoupled from the spatial Cartesian grids. As shown in Eqs. (26) and (27), the evaluations of the moments of g^{eq} and h^{eq} need a GHQ of sixth-order accuracy and fourth-order accuracy, respectively. Since the GHQ accuracy is typically given at odd orders, we adopt D3V27A7 [21,22] with 27 discrete particle velocities and seventh-order GHQ accuracy, and D3V13A5 [22] with 13 discrete particle velocities and the fifth-order GHQ accuracy. The reasons for using these particle velocity models are explained in detail in Refs. [19,20]. The relevant symmetric group of discrete velocity vectors, number in each group, and associated weights for D3V13A5 and D3V27A7 are summarized in Table III.

APPENDIX B: THE CHAPMAN-ENSKOG-EXPANSION–BASED LIFTING RELATION AND THE HERMITE-EXPANSION–BASED LIFTING RELATION FOR QI *ET AL.*'S TOTAL ENERGY DDF MODEL

Here we provide a brief but sufficient introduction for Qi *et al.*'s model [19]. The kinetic equation in Eq. (5) of Qi *et al.*'s model is replaced by the Boltzmann-BGK equation with a source term as

$$\partial_t f + \boldsymbol{\xi}\cdot\nabla f + \boldsymbol{b}\cdot\nabla_{\boldsymbol{\xi}} f = \frac{f^{\mathrm{eq}} - f}{\tau} + S_f. \tag{B1}$$

The source term S_f may alter the microscopic physics, but with the advantages of preserving the simplicity of the Boltzmann-BGK collision term and at the same time correctly recovering the general NSF system of the original Boltzmann equation in the continuum limit. Although the equilibrium, the conservative variables, the viscous stress, the heat flux, and two reduced

distribution functions with their equilibria are the same as before, Eq. (B1) can be converted as two Boltzmann equations sharing the same relaxation time, namely

$$\partial_t g + \boldsymbol{\xi}\cdot\nabla g + \boldsymbol{b}\cdot\nabla_{\boldsymbol{\xi}} g = \frac{g^{\mathrm{eq}} - g}{\tau} + S_g, \tag{B2a}$$

$$\partial_t h + \boldsymbol{\xi}\cdot\nabla h + \boldsymbol{b}\cdot\nabla_{\boldsymbol{\xi}} h = \boldsymbol{b}\cdot\boldsymbol{\xi} g + \frac{h^{\mathrm{eq}} - h}{\tau} + S_h, \tag{B2b}$$

where S_g and S_h are the integrated source terms of S_f, respectively. By assuming that τ has a small magnitude, we carry out the CE analysis on Eq. (B2) for recovering the macroscopic equations, and we obtain

$$g = g^{\mathrm{eq}} - \tau\left(\partial_t g^{\mathrm{eq}} + \boldsymbol{\xi}\cdot\nabla g^{\mathrm{eq}} - \frac{\boldsymbol{b}\cdot\boldsymbol{c}}{RT} g^{\mathrm{eq}} - S_g\right) + O(\tau^2), \tag{B3a}$$

$$h = h^{\mathrm{eq}} - \tau\left(\partial_t h^{\mathrm{eq}} + \boldsymbol{\xi}\cdot\nabla h^{\mathrm{eq}} - \frac{\boldsymbol{b}\cdot\boldsymbol{c}}{RT} h^{\mathrm{eq}} - S_h\right) + O(\tau^2). \tag{B3b}$$

By taking the zeroth- and the first-order velocity moment of Eq. (B3a) up to the order of $O(1)$ for the mass conservation and the momentum conservation at the Euler level, we can find the first two velocity moment constraints for the source terms

$$\int S_g d\boldsymbol{\xi} = 0, \quad \int \boldsymbol{\xi} S_g d\boldsymbol{\xi} = \boldsymbol{0}. \tag{B4}$$

Moreover, we take the zeroth-order velocity moment of Eq. (B3b) up to the order of $O(1)$ for the energy equation at the Euler level, the third constraint for the source terms can be derived as $\int S_h d\boldsymbol{\xi} = 0$. Take the $O(\tau)$ approximation of Eq. (B3) into Eq. (12), the viscosity stress and the heat flux at the NSF level can be expressed as

$$\boldsymbol{\sigma} = \tau \int \boldsymbol{cc}\left(\frac{\partial g^{\mathrm{eq}}}{\partial t} + \boldsymbol{\xi}\cdot\nabla g^{\mathrm{eq}} - \frac{\boldsymbol{b}\cdot\boldsymbol{c}}{RT} g^{\mathrm{eq}} - S_g\right) d\boldsymbol{\xi} + O(\tau^2), \tag{B5a}$$

$$\boldsymbol{q} = -\tau \int \boldsymbol{c}\left[\left(\frac{u^2}{2} - \boldsymbol{u}\cdot\boldsymbol{\xi}\right)\left(\partial_t g^{\mathrm{eq}} + \boldsymbol{\xi}\cdot\nabla g^{\mathrm{eq}} - \frac{\boldsymbol{b}\cdot\boldsymbol{c}}{RT} g^{\mathrm{eq}} - S_g\right) + \left(\partial_t h^{\mathrm{eq}} + \boldsymbol{\xi}\cdot\nabla h^{\mathrm{eq}} - \frac{\boldsymbol{b}\cdot\boldsymbol{c}}{RT} h^{\mathrm{eq}} - S_h\right)\right] d\boldsymbol{\xi} + O(\tau^2). \tag{B5b}$$

With the help of the Euler equations Eq. (1) in the order of $O(1)$, all the derivatives of g^{eq} and h^{eq} are transformed into the products of equilibria with the hydrodynamics variables and their derivatives as

$$\partial_t g^{\mathrm{eq}} + \boldsymbol{\xi}\cdot\nabla g^{\mathrm{eq}} - \frac{\boldsymbol{b}\cdot\boldsymbol{c}}{RT} g^{\mathrm{eq}} = g^{\mathrm{eq}}\left[\left(\frac{c^2}{2RT} - \frac{D+2}{2}\right)\boldsymbol{c}\cdot\nabla(\ln T) + \frac{\boldsymbol{c}\cdot\nabla\boldsymbol{u}\cdot\boldsymbol{c}}{RT} - \left(\frac{c^2}{RT} + K + 3 - D\right)\frac{\vartheta}{K+3}\right], \tag{B6a}$$

$$\begin{aligned}\partial_t h^{\mathrm{eq}} + \boldsymbol{\xi}\cdot\nabla h^{\mathrm{eq}} - \frac{\boldsymbol{b}\cdot\boldsymbol{c}}{RT} h^{\mathrm{eq}} = {} & h^{\mathrm{eq}}\left[\left(\frac{c^2}{2RT} - \frac{D+2}{2}\right)\boldsymbol{c}\cdot\nabla(\ln T) + \frac{\boldsymbol{c}\cdot\nabla\boldsymbol{u}\cdot\boldsymbol{c}}{RT} - \left(\frac{c^2}{RT} + K + 3 - D\right)\frac{\vartheta}{K+3}\right] \\ & + g^{\mathrm{eq}}\frac{(3-D+K)RT}{2}\left(\vec{c}\cdot\nabla(\ln T) - \frac{2\vartheta}{K+3}\right).\end{aligned} \tag{B6b}$$

Take the above expansions along with the constitutive laws in Eq. (3), we could obtain two additional constraints for the source terms, namely

$$\int \boldsymbol{\xi}\boldsymbol{\xi} S_g d\boldsymbol{\xi} = \left(\frac{2}{D} - \frac{2}{K+3} - \frac{\mu_V}{\mu}\right) p\vartheta \boldsymbol{I}, \quad \int \boldsymbol{\xi} S_h d\boldsymbol{\xi} = \left(\frac{2}{D} - \frac{2}{K+3} - \frac{\mu_V}{\mu}\right) p\vartheta \boldsymbol{u} + p\left(1 - \frac{1}{\mathrm{Pr}}\right)\frac{(K+5)R}{2}\nabla T. \tag{B7}$$

With the five velocity moment constraints for the source terms, we can construct the second-order Hermite expansion for S_g and the first-order Hermite expansion for S_h as follows:

$$S_g = (S_g)^{(2)} = \frac{\exp\left(-\frac{\xi^2}{2RT_0}\right)}{(2\pi RT_0)^{D/2}}\left(\frac{\xi^2}{RT_0} - D\right)\left(\frac{2}{D} - \frac{2}{K+3} - \chi\right)\frac{p\vartheta}{2RT_0}, \tag{B8a}$$

$$S_h = (S_h)^{(1)} = \frac{\exp\left(-\frac{\xi^2}{2RT_0}\right)}{(2\pi RT_0)^{D/2}}\left[\left(\frac{2}{D} - \frac{2}{K+3} - \chi\right)\frac{\boldsymbol{\xi}\cdot\boldsymbol{u}}{RT_0} p\vartheta + \left(1 - \frac{1}{\mathrm{Pr}}\right)\frac{K+5}{2}\frac{p}{T_0}\boldsymbol{\xi}\cdot\nabla T\right]. \tag{B8b}$$

After the establishment of Qi *et al.*'s model, we here introduce the numerical implementations. We only replace the ϕ' by the $\phi^{\mathrm{eq}} + \tau S_\phi$, and keep the rest in Sec. II C unchanged. Moreover, the dilatation terms in S_ϕ is evaluated by a fourth-order central finite difference.

The Hermite-expansion–based lifting relations for both model are the same since the velocity moment constraints are not changed, however, the Chapman-expansion–based lifting relations from Eq. (B3) up to the order of $O(\tau)$ need to be updated to yield

$$g^{\mathrm{CE},Qi} = g^{eq}\left\{1-\tau\left[\left(\frac{c^2}{2RT}-\frac{D+2}{2}\right)\boldsymbol{c}\cdot\boldsymbol{\nabla}(\ln T)+\frac{\boldsymbol{c}\cdot\boldsymbol{\nabla}\boldsymbol{u}\cdot\boldsymbol{c}}{RT}-\left(\frac{c^2}{RT}+K+3-D\right)\frac{\vartheta}{K+3}\right]\right\}+\tau S_g, \tag{B9a}$$

$$h^{\mathrm{CE},Qi} = h^{eq}-\tau\left\{\begin{aligned}&h^{eq}\left[\left(\frac{c^2}{2RT}-\frac{D+2}{2}\right)\boldsymbol{c}\cdot\boldsymbol{\nabla}(\ln T)+\frac{\boldsymbol{c}\cdot\boldsymbol{\nabla}\boldsymbol{u}\cdot\boldsymbol{c}}{RT}-\left(\frac{c^2}{RT}+K+3-D\right)\frac{\vartheta}{K+3}\right]\\&+g^{eq}\,\frac{(3-D+K)RT}{2}\left[\boldsymbol{c}\cdot\boldsymbol{\nabla}(\ln T)+\frac{2\vartheta}{K+3}\right]\end{aligned}\right\}+\tau S_h. \tag{B9b}$$

We note that g needs the 10th-order GHQ accuracy for the viscous stress and the 4th-order GHQ accuracy for the heat flux, while h required the 8th-order GHQ accuracy for the heat flux. Moreover, if the initial dilatation and the temperature gradient are zero, then the order of accuracy will reduce to the 4th-order GHQ accuracy for g and the 6th-order GHQ accuracy for h.

To test both lifting relations in different kinetic models, we take the same parameters as the cases of Sec. IV B except for the $\chi = 0$ according to the reference [35]. We compare the results based on initialization done by different lifting relations and at different resolutions, and the curves from different lifting relations overlap with each other at the same resolution. The evolution of total kinetic energy, solenoidal dissipation, and total dissipation (not shown here) are nearly identical to the results from Guo *et al.*'s model at the same resolution, already discussed in the main body of the paper. This observation illustrates that the bulk viscosity effects can be neglected for the evolution of total kinetic energy, solenoidal dissipation, and total dissipation. But in the compressive dissipation, the bulk viscosity plays an important role. From Fig. 4(a), the time evolution of compressive dissipation in Qi *et al.*'s model at the highest resolution is close but slightly below the reference curve. Compared the compressive dissipation and the solenoidal dissipation at 256^3 with the reference, we find that resolving the vortical structures requires more grids than the compressive motion. In short, the results in Qi *et al.*'s model are in good agreement with the literature.

APPENDIX C: THE SIXTH-ORDER TENO SCHEME FOR RECONSTRUCTION OF DISTRIBUTION FUNCTIONS AT CELL INTERFACE

If the sets of discrete particle velocity model are chosen, then the Boltzmann-BGK equation will become a set of finite-number linear advection equations. We implement the sixth-order TENO [23] scheme to reconstruct the cell-interface particle distribution function $\bar{\phi}^{+}(\boldsymbol{x}_b, \boldsymbol{\xi}_\alpha, t_n)$ by using the cell-averaged value $\bar{\phi}_j^{+,n}(\boldsymbol{\xi}_\alpha)$. To stabilize our numerical reconstruction, the upwind rule is utilized depending on the direction of a discrete particle velocity.

Take the x-direction reconstruction of the particle distribution function at cell interface $x_{j+1/2}$ with $\xi_{\alpha,x} > 0$ as an example, we divide the stencil with six cells into four adjacent substencils and interpolate for $\bar{\phi}^{+}(x_{j+1/2}, \boldsymbol{\xi}_\alpha, t_n)$, using

$$\bar{\phi}^{+,(0)}(x_{j+1/2}, \boldsymbol{\xi}_\alpha, t_n) = -\frac{1}{6}\bar{\phi}_{j-1}^{+,n}(\boldsymbol{\xi}_\alpha)+\frac{5}{6}\bar{\phi}_{j}^{+,n}(\boldsymbol{\xi}_\alpha)+\frac{1}{3}\bar{\phi}_{j+1}^{+,n}(\boldsymbol{\xi}_\alpha), \tag{C1a}$$

$$\bar{\phi}^{+,(1)}(x_{j+1/2}, \boldsymbol{\xi}_\alpha, t_n) = \frac{1}{3}\bar{\phi}_{j}^{+,n}(\boldsymbol{\xi}_\alpha)+\frac{5}{6}\bar{\phi}_{j+1}^{+,n}(\boldsymbol{\xi}_\alpha)-\frac{1}{6}\bar{\phi}_{j+2}^{+,n}(\boldsymbol{\xi}_\alpha), \tag{C1b}$$

$$\bar{\phi}^{+,(2)}(x_{j+1/2}, \boldsymbol{\xi}_\alpha, t_n) = \frac{1}{3}\bar{\phi}_{j-2}^{+,n}(\boldsymbol{\xi}_\alpha)-\frac{7}{6}\bar{\phi}_{j-1}^{+,n}(\boldsymbol{\xi}_\alpha)+\frac{11}{6}\bar{\phi}_{j}^{+,n}(\boldsymbol{\xi}_\alpha), \tag{C1c}$$

$$\bar{\phi}^{+,(3)}(x_{j+1/2}, \boldsymbol{\xi}_\alpha, t_n) = \frac{1}{4}\bar{\phi}_{j}^{+,n}(\boldsymbol{\xi}_\alpha)+\frac{13}{12}\bar{\phi}_{j+1}^{+,n}(\boldsymbol{\xi}_\alpha)-\frac{5}{12}\bar{\phi}_{j+2}^{+,n}(\boldsymbol{\xi}_\alpha)+\frac{1}{12}\bar{\phi}_{j+3}^{+,n}(\boldsymbol{\xi}_\alpha), \tag{C1d}$$

where the superscripts of $\bar{\phi}^{+}(x_{j+1/2}, \boldsymbol{\xi}, t_n)$ denote the sequence of substencils. The smoothness factor β_0, β_1, β_2, and β_3 for the four substencils can be obtained by

$$\beta_0 = \frac{13}{12}\left[\bar{\phi}_{j-1}^{+,n}(\boldsymbol{\xi}_\alpha)-2\bar{\phi}_{j}^{+,n}(\boldsymbol{\xi}_\alpha)+\bar{\phi}_{j+1}^{+,n}(\boldsymbol{\xi}_\alpha)\right]^2+\frac{1}{4}\left[\bar{\phi}_{j+1}^{+,n}(\boldsymbol{\xi}_\alpha)-\bar{\phi}_{j-1}^{+,n}(\boldsymbol{\xi}_\alpha)\right]^2, \tag{C2a}$$

$$\beta_1 = \frac{13}{12}\left[\bar{\phi}_{j}^{+,n}(\boldsymbol{\xi}_\alpha)-2\bar{\phi}_{j+1}^{+,n}(\boldsymbol{\xi}_\alpha)+\bar{\phi}_{j+2}^{+,n}(\boldsymbol{\xi}_\alpha)\right]^2+\frac{1}{4}\left[3\bar{\phi}_{j}^{+,n}(\boldsymbol{\xi}_\alpha)-4\bar{\phi}_{j+1}^{+,n}(\boldsymbol{\xi}_\alpha)+\bar{\phi}_{j+2}^{+,n}(\boldsymbol{\xi}_\alpha)\right]^2, \tag{C2b}$$

$$\beta_2 = \frac{13}{12}\left[\bar{\phi}_{j-2}^{+,n}(\boldsymbol{\xi}_\alpha)-2\bar{\phi}_{j-1}^{+,n}(\boldsymbol{\xi}_\alpha)+\bar{\phi}_{j}^{+,n}(\boldsymbol{\xi}_\alpha)\right]^2+\frac{1}{4}\left[\bar{\phi}_{j-2}^{+,n}(\boldsymbol{\xi}_\alpha)-4\bar{\phi}_{j-1}^{+,n}(\boldsymbol{\xi}_\alpha)+3\bar{\phi}_{j}^{+,n}(\boldsymbol{\xi}_\alpha)\right]^2, \tag{C2c}$$

$$\begin{aligned}\beta_3 = {}&\bar{\phi}_{j}^{+,n}(\boldsymbol{\xi}_\alpha)\left[2107\bar{\phi}_{j}^{+,n}(\boldsymbol{\xi}_\alpha)-9402\bar{\phi}_{j+1}^{+,n}(\boldsymbol{\xi}_\alpha)+7042\bar{\phi}_{j+2}^{+,n}(\boldsymbol{\xi}_\alpha)-1854\bar{\phi}_{j+3}^{+,n}(\boldsymbol{\xi}_\alpha)\right]\\&+\bar{\phi}_{j+1}^{+,n}(\boldsymbol{\xi}_\alpha)\left[11003\bar{\phi}_{j+1}^{+,n}(\boldsymbol{\xi}_\alpha)-17246\bar{\phi}_{j+2}^{+,n}(\boldsymbol{\xi}_\alpha)+4642\bar{\phi}_{j+3}^{+,n}(\boldsymbol{\xi}_\alpha)\right]\\&+\bar{\phi}_{j+2}^{+,n}(\boldsymbol{\xi}_\alpha)\left[7043\bar{\phi}_{j+2}^{+,n}(\boldsymbol{\xi}_\alpha)-3882\bar{\phi}_{j+3}^{+,n}(\boldsymbol{\xi}_\alpha)\right]+547\left[\bar{\phi}_{j+3}^{+,n}(\boldsymbol{\xi}_\alpha)\right]^2.\end{aligned} \tag{C2d}$$

The nonlinear weights of the sixth-order TENO can be evaluated by

$$\omega_j = \frac{\gamma_j\delta_j}{\sum_{k=0}^{3}\gamma_k\delta_k},\quad \tilde{\gamma}_j = \left[C+\frac{\beta_3-(\beta_0+\beta_2+4\beta_1)/6}{\beta_j+\epsilon_0}\right]^p,\quad \tilde{\omega}_j = \frac{\tilde{\gamma}_j}{\sum_{k=0}^{3}\tilde{\gamma}_k},\quad \delta_j = \begin{cases}0, \text{ if } \tilde{\omega}_j < \epsilon_T,\\ 1, \text{ otherwise,}\end{cases} \tag{C3}$$

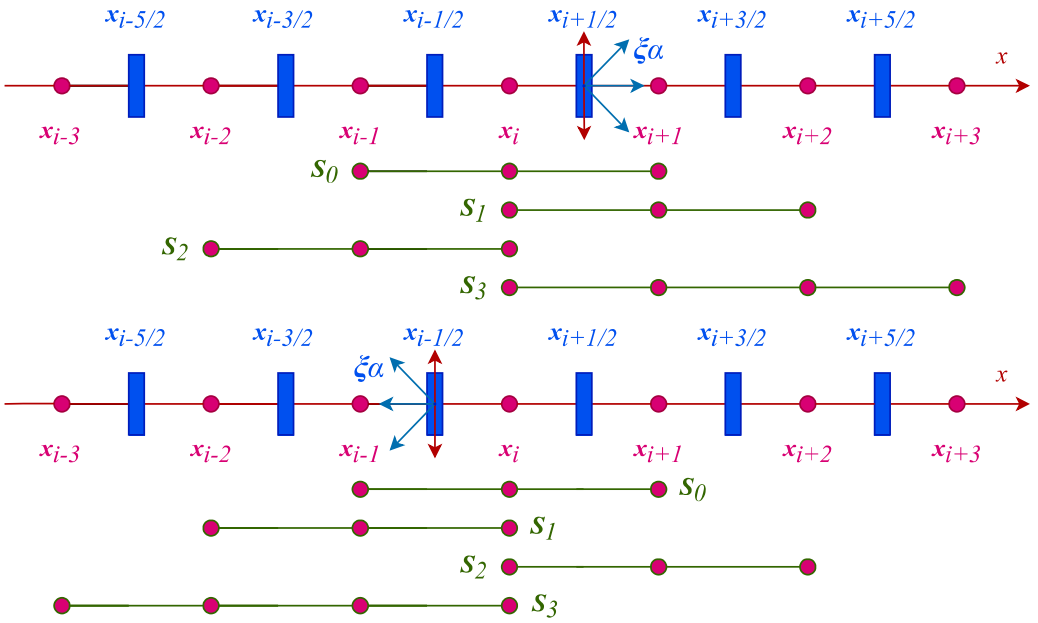

FIG. 5. Reconstruction of cell-interface particle distribution functions with the sixth-order TENO scheme.

where $\gamma_0 = 0.462$, $\gamma_1 = 0.3$, $\gamma_1 = 0.054$, and $\gamma_3 = 0.184$ are the optimal weights. The parameters $C = 1.0$ and $p = 6$ are applied for robustly separating the resolved scales from the nonresolved. A small number $\epsilon_0 = 10^{-40}$ avoids zero occurring in the denominator. $\epsilon_T = 10^{-7}$ is a cutoff threshold to suppress the substencils without enough smoothness. Those values above are all set as suggested [23]. Then $\bar{\phi}^+(x_{j+1/2}, \boldsymbol{\xi}_\alpha, t_n)$ is calculated by

$$\bar{\phi}^+(x_{j+1/2}, \boldsymbol{\xi}_\alpha, t_n) = \sum_{k=0}^{3} \omega_k \bar{\phi}^{+,(k)}(x_{j+1/2}, \boldsymbol{\xi}_\alpha, t_n). \tag{C4}$$

If $\xi_{\alpha,x} < 0$ at the cell interface $x_{j+1/2}$, then we execute the similar procedure with three substencils in the upwind direction. If $\xi_{\alpha,x} = 0$, then we take the average of the results from the above-mentioned cases. The whole diagram of reconstruction is shown in Fig. 5, and the technique is similar for the cell interfaces in then y and z directions.

For the compressible turbulence simulation, the numerical schemes are required to resolve small-scale flow structures and capture discontinuities simultaneously. The former demand means low numerical dissipation for resolving small-scale flow characters while the latter demand insists sufficient numerical dissipation to handle discontinuities. The well-established WENO schemes are robust for many situations; however, they exhibit excessive dissipation that significantly damps out the small-scale structures. With the benefits of essentially-non-oscillatory-like stencil selection, we choose TENO scheme for its robustness for discontinuities and lower numerical dissipation than the popular WENO schemes.

APPENDIX D: CONSTRUCTION OF THE HERMITE POLYNOMIALS

We provide a brief yet complete background of the Hermite expansion. The nth-order Hermite polynomial in high dimensions [27] is given by

$$\mathcal{H}^{(n)}(\boldsymbol{\xi}, T_0) = (\sqrt{RT_0})^n \frac{(-1)^n}{\omega(\boldsymbol{\xi}, T_0)} \underbrace{\nabla_{\boldsymbol{\xi}} \cdots \nabla_{\boldsymbol{\xi}}}_{\text{n-fold}} \omega(\boldsymbol{\xi}, T_0), \tag{D1}$$

where $\omega(\boldsymbol{\xi}, T_0) = \exp(-\xi^2/(2RT_0))/(2\pi RT_0)^{D/2}$ is the weighting function and T_0 is the constant reference temperature and $\nabla_{\boldsymbol{\xi}}$ is the nabla operator in space of $\boldsymbol{\xi}$. We adopt Grad's short-hand notation [27] to represent the symmetric tensor, and the nth-order polynomial is

$$\mathcal{H}^{(n)}(\boldsymbol{\xi}, T_0) = \left(\frac{\boldsymbol{\xi}}{\sqrt{RT_0}}\right)^n - \left(\frac{\boldsymbol{\xi}}{\sqrt{RT_0}}\right)^{n-2} \boldsymbol{I} + \left(\frac{\boldsymbol{\xi}}{\sqrt{RT_0}}\right)^{n-4} \boldsymbol{I}^2 - \cdots, \tag{D2}$$

where $(\frac{\boldsymbol{\xi}}{\sqrt{RT_0}})^{n-2m}\boldsymbol{I}^m$ contains a total of $\frac{n!}{2^m m!(n-2m)!}$ terms. For example, $(\frac{\boldsymbol{\xi}}{\sqrt{RT_0}})\boldsymbol{I} = \frac{\xi_i I_{jk}}{\sqrt{RT_0}} + \frac{\xi_j I_{ik}}{\sqrt{RT_0}} + \frac{\xi_k I_{ij}}{\sqrt{RT_0}}$. The recurrence relation of the Hermite polynomials can be obtained in Grad's short-hand notation as

$$\frac{\xi_i}{\sqrt{RT_0}} \mathcal{H}^{(n)}(\boldsymbol{\xi}) = \mathcal{H}^{(n+1)}(\boldsymbol{\xi}) + \boldsymbol{I}_i \mathcal{H}^{(n-1)}(\boldsymbol{\xi}), \tag{D3}$$

which is equivalent to

$$\frac{\xi_i}{\sqrt{RT_0}}\mathcal{H}^{(n)}_{i_1 i_2\cdots i_n} = \mathcal{H}^{(n+1)}_{i i_1 i_2\cdots i_n} + \sum_{k=1}^{n} I_{i i_k}\mathcal{H}^{(n-1)}_{i_1 i_2\cdots i_{k-1} i_{k+1}\cdots i_n}. \tag{D4}$$

The orthogonality of the Hermite polynomials can be shown as

$$\int \omega(\boldsymbol{\xi}, T_0)\mathcal{H}^m_{\boldsymbol{i}}(\boldsymbol{\xi}, T_0)\mathcal{H}^n_{\boldsymbol{j}}(\boldsymbol{\xi}, T_0)d\boldsymbol{\xi} = \delta_{mn}\delta^n_{\boldsymbol{ij}}, \tag{D5}$$

where $\boldsymbol{i}$ denotes the sequence $i_1\cdots i_n$, and $\delta^n_{\boldsymbol{ij}}$ equals to 1 if and only if $\boldsymbol{i}$ is the permutation of $\boldsymbol{j}$. We evaluate function $f(\boldsymbol{x}, \boldsymbol{\xi}, t)$ with the nth-order Hermite expansion $f^{(N)}(\boldsymbol{x}, \boldsymbol{\xi}, t)$ in the following sense:

$$f(\boldsymbol{x}, \boldsymbol{\xi}, t) \approx f^{(N)}(\boldsymbol{x}, \boldsymbol{\xi}, t) = \omega(\boldsymbol{\xi}, T_0)\sum_{k=0}^{N}\frac{1}{k!}a^{(k)}_{\boldsymbol{i}}(\boldsymbol{x}, t, T_0)\mathcal{H}^{(k)}_{\boldsymbol{i}}(\boldsymbol{\xi}, T_0), \tag{D6}$$

where the Hermite expansion coefficient can be found as

$$a^{(k)}_{\boldsymbol{i}}(\boldsymbol{x}, t, T_0) = \int f(\boldsymbol{x}, \boldsymbol{\xi}, t)\mathcal{H}^{(k)}_{\boldsymbol{i}}(\boldsymbol{\xi}, T_0)d\boldsymbol{\xi}. \tag{D7}$$

The formulas in Eq. (14), Eq. (28), and Eq. (30) are all constructed from the velocity moments by the Hermite expansion.

APPENDIX E: THE HERMITE EXPANSIONS OF THE EXTERNAL FORCE TERMS

In this part, the Hermite expansions of the external force terms for both Guo *et al.*'s model [16] and Qi *et al.*'s model [19] are presented here. To recover the mass and momentum conservations for Guo *et al.*'s model at the NSF level from the reduced Boltzmann-BGK equation for g, Eq. (10a), the velocity moments of the force terms can be obtained as

$$\int(\boldsymbol{b}\cdot\nabla_{\boldsymbol{\xi}}g)d\boldsymbol{\xi} = 0, \quad \int\boldsymbol{\xi}(\boldsymbol{b}\cdot\nabla_{\boldsymbol{\xi}}g)d\boldsymbol{\xi} = \rho\boldsymbol{b}, \quad \int\xi_i\xi_j(\boldsymbol{b}\cdot\nabla_{\boldsymbol{\xi}}g)d\boldsymbol{\xi} = \rho(b_iu_j + b_ju_i). \tag{E1}$$

Based on the reduced Boltzmann-BGK equation for h, Eq. (10b), recovering the energy equation at the NSF level requires two velocity moments as follows:

$$\int(\boldsymbol{b}\cdot\nabla_{\boldsymbol{\xi}}h - \boldsymbol{b}\cdot\boldsymbol{\xi}g)d\boldsymbol{\xi} = \rho\boldsymbol{u}\cdot\boldsymbol{b}, \quad \int\boldsymbol{\xi}(\boldsymbol{b}\cdot\nabla_{\boldsymbol{\xi}}h - \boldsymbol{b}\cdot\boldsymbol{\xi}g)d\boldsymbol{\xi} = \rho\boldsymbol{u}\boldsymbol{u}\cdot\boldsymbol{b} + (\rho E + p)\boldsymbol{b}. \tag{E2}$$

By setting all the higher moments to zero, the truncated Hermite expansions for the force terms (see Appendix D) are

$$(\boldsymbol{b}\cdot\nabla_{\boldsymbol{\xi}}g)^{(2)} = \frac{\omega(\boldsymbol{\xi}, T_0)\rho}{RT_0}\left(\boldsymbol{b}\cdot\boldsymbol{c} + \boldsymbol{b}\cdot\boldsymbol{\xi}\frac{\boldsymbol{\xi}\cdot\boldsymbol{u}}{RT_0}\right), \tag{E3a}$$

$$(\boldsymbol{b}\cdot\nabla_{\boldsymbol{\xi}}h - \boldsymbol{b}\cdot\boldsymbol{\xi}g)^{(1)} = \omega(\boldsymbol{\xi}, T_0)\left[\rho\boldsymbol{u}\cdot\boldsymbol{b} + \rho\boldsymbol{b}\cdot\boldsymbol{u}\frac{\boldsymbol{u}\cdot\boldsymbol{\xi}}{\sqrt{RT_0}} + (\rho E + p)\frac{\boldsymbol{b}\cdot\boldsymbol{\xi}}{\sqrt{RT_0}}\right]. \tag{E3b}$$

The conversion from the continuous space-time Boltzmann equation to the lattice Boltzmann equation is done by integrating the continuous Boltzmann equation along the characteristic line using the trapezoidal rule; in this process a transformation is applied to convert the resulting implicit scheme to an explicit form [5]. This additional process adds an additional factor $[1 - 1/(2\tau_L)^{-1}]$ where $\tau_L = \tau_g/\Delta t + 1/2$, then it will render Eq. (E3a) identical to the expression derived in Guo *et al.* [16]. A similar procedure can be performed for Qi *et al.*'s model [19]. The force terms in Qi *et al.*'s model have the same Hermite expansions as those described in Eq. (E3) since recovering the external force terms at the NSF level from the reduced Boltzmann-BGK equations Eqs. (B2a) and (B2b) requires the same velocity moments.

[1] S. Chen and G. D. Doolen, Lattice Boltzmann method for fluid flows, Annu. Rev. Fluid Mech. **30**, 329 (1998).

[2] K. Xu and J.-C. Huang, A unified gas-kinetic scheme for continuum and rarefied flows, J. Comput. Phys. **229**, 7747 (2010).

[3] Z. Guo, K. Xu, and R. Wang, Discrete unified gas kinetic scheme for all Knudsen number flows: Low-speed isothermal case, Phys. Rev. E **88**, 033305 (2013).

[4] H. Xu, H. Luan, Y. He, and W. Tao, A lifting relation from macroscopic variables to mesoscopic variables in lattice Boltzmann method: Derivation, numerical assessments and coupling computations validation, Comput. Fluids **54**, 92 (2012).

[5] Z.-Q. Dong, L.-P. Wang, C. Peng, and T. Chen, A systematic study of hidden errors in the bounce-back scheme and their various effects in the lattice Boltzmann simulation of viscous flows, Phys. Fluids **34**, 093608 (2022).

[6] R. Mei, L.-S. Luo, P. Lallemand, and D. d'Humieères, Consistent initial conditions for lattice Boltzmann simulations, Comput. Fluids **35**, 855 (2006).

[7] T. Krüger, F. Varnik, and D. Raabe, Second-order convergence of the deviatoric stress tensor in the standard Bhatnagar-Gross-Krook lattice Boltzmann method, Phys. Rev. E **82**, 025701(R) (2010).

[8] Z.-X. Tong, M.-J. Li, X. Chen, and Y.-L. He, Direct coupling between molecular dynamics and lattice Boltzmann method based on velocity distribution functions for steady-state isothermal flow, Int. J. Heat Mass Transf. **115**, 544 (2017).

[9] P. A. Skordos, Initial and boundary conditions for the lattice Boltzmann method, Phys. Rev. E **48**, 4823 (1993).

[10] T. Imamura, K. Suzuki, T. Nakamura, and M. Yoshida, Acceleration of steady-state lattice Boltzmann simulations on non-uniform mesh using local time step method, J. Comput. Phys. **202**, 645 (2005).

[11] Z.-X. Tong and Y.-L. He, A unified coupling scheme between lattice Boltzmann method and finite volume method for unsteady fluid flow and heat transfer, Int. J. Heat Mass Transf. **80**, 812 (2015).

[12] P. Van Leemput, W. Vanroose, and D. Roose, Mesoscale analysis of the equation-free constrained runs initialization scheme, Multiscale Model. Simul. **6**, 1234 (2008).

[13] P. L. Bhatnagar, E. P. Gross, and M. Krook, A model for collision processes in gases. I. Small amplitude processes in charged and neutral one-component systems, Phys. Rev. **94**, 511 (1954).

[14] Z.-X. Tong, M.-J. Li, Y.-L. He, and W.-Q. Tao, Analysis and numerical tests of lifting relations to reconstruct LBM distribution functions for coupling simulations, Int. J. Heat Mass Transf. **107**, 945 (2017).

[15] M. R. Salimi and M. Taeibi-Rahni, New lifting relations for estimating LBM distribution functions from corresponding macroscopic quantities, based on equilibrium and non-equilibrium moments, J. Comput. Phys. **302**, 155 (2015).

[16] Z. Guo, C. Zheng, B. Shi, and T. S. Zhao, Thermal lattice Boltzmann equation for low Mach number flows: Decoupling model, Phys. Rev. E **75**, 036704 (2007).

[17] X. Nie, X. Shan, and H. Chen, Thermal lattice Boltzmann model for gases with internal degrees of freedom, Phys. Rev. E **77**, 035701(R) (2008).

[18] X. Wen, L.-P. Wang, and Z. Guo, Designing a consistent implementation of the discrete unified gas-kinetic scheme for the simulation of three-dimensional compressible natural convection, Phys. Fluids **33**, 046101 (2021).

[19] Y. Qi, T. Chen, L.-P. Wang, Z. Guo, and S. Chen, An efficient discrete unified gas-kineticscheme for compressible turbulence, Phys. Fluids **34**, 116101 (2022).

[20] Z. Guo, L.-P. Wang, and Y. Qi, Discrete unified gas kinetic scheme for continuum compressible flows, Phys. Rev. E **107**, 025304 (2023).

[21] A. H. Stroud, *Approximate Calculation of Multiple Integrals*, Prentice-Hall Series in Automatic Computation (Prentice-Hall, Hoboken, NJ, 1971).

[22] X. Shan, X.-F. Yuan, and H. Chen, Kinetic theory representation of hydrodynamics: A way beyond the Navier-Stokes equation, J. Fluid Mech. **550**, 413 (2006).

[23] L. Fu, X. Y. Hu, and N. A. Adams, A family of high-order targeted ENO schemes for compressible-fluid simulations, J. Comput. Phys. **305**, 333 (2016).

[24] W. Sutherland, LII. The viscosity of gases and molecular force, Lond. Edinb. Dubl. Philos. Mag. J. Sci. **36**, 507 (1893).

[25] T. Chen, L.-P. Wang, J. Lai, and S. Chen, Inverse design of mesoscopic models forcompressible flow using the Chapman-Enskog analysis, Adv. Aerodynam. **3**, 5 (2021).

[26] R. Zhang, X. Shan, and H. Chen, Efficient kinetic method for fluid simulation beyond the Navier-Stokes equation, Phys. Rev. E **74**, 046703 (2006).

[27] H. Grad, Note on N-dimensional Hermite polynomials, Commun. Pure Appl. Math. **2**, 325 (1949).

[28] B. Van Leer, Towards the ultimate conservative difference scheme. IV. A new approach to numerical convection, J. Comput. Phys. **23**, 276 (1977).

[29] R. Borges, M. Carmona, B. Costa, and W. S. Don, An improved weighted essentially non-oscillatory scheme for hyperbolic conservation laws, J. Comput. Phys. **227**, 3191 (2008).

[30] G. I. Taylor and A. E. Green, Mechanism of the production of small Eddies from large ones, Proc. Roy. Soc. Lond. Ser. A Math. Phys. Sci. **158**, 499 (1937).

[31] W. M. van Rees, A. Leonard, D. I. Pullin, and P. Koumoutsakos, A comparison of vortex and pseudo-spectral methods for the simulation of periodic vortical flows at high Reynolds numbers, J. Comput. Phys. **230**, 2794 (2011).

[32] H. B. Squire and R. V. Southwell, On the stability for three-dimensional disturbances of viscous fluid flow between parallel walls, Proc. Roy. Soc. Lond. Se. A **142**, 621 (1933).

[33] J.-Z. Wu, H.-Y. Ma, and M.-D. Zhou, *Vortical Flows*, 1st ed. (Springer, Berlin, 2015).

[34] R. H. Dishington, Rate of surface-strain tensor, Am. J. Phys. **33**, 827 (1965).

[35] D. J. Lusher and N. D. Sandham, Assessment of low-dissipative shock-capturing schemes for the compressible Taylor-Green vortex, AIAA J. **59**, 533 (2021).

[36] Z. Guo, T. S. Zhao, and Y. Shi, Preconditioned lattice-Boltzmann method forsteady flows, Phys. Rev. E **70**, 066706 (2004).